TÉCNICO LISBOA

Development of a population balance modelling for predicting bubble size distribution dynamics

Diogo Alexandre dos Santos Abreu

Thesis to obtain the Master of Science Degree in

Biological Engineering

Supervisors: Prof. Ingmar Nopens
Prof. Luís Joaquim Pina da Fonseca

Examination Committee

Chairperson: Prof. Marília Clemente Velez Mateus
Supervisor: Prof. Luís Joaquim Pina da Fonseca
Members of the Committee: Prof. Sebastião Manuel Tavares da Silva Alves
Eng. Andreia Neves do Amaral

November 2018

Preface

The work presented in this thesis was performed at Biomath of Ghent University, during the period February - November of 2018, under the supervision of Professor Ingmar Nopens and researcher Andreia Amaral. The thesis was co-supervised at Instituto Superior Técnico by Professor Luís Fonseca.

Agradecimentos

Em primeiro lugar, quero agradecer ao Professor Ingmar Nopens por me ter dado a oportunidade de estudar no seu grupo de investigação. A sua ajuda e disponibilidade foram sempre impecáveis e este documento não seria possível sem elas. Quero também estender os meus agradecimentos à Engenheira Andreia Amaral e ao Senhor Engenheiro Juan Pablo Gallo Molina por me terem guiado nestes últimos meses. Sem eles, este documento não teria sido finalizado.

A minha gratidão está também com a minha família, principalmente com a minha mãe, Clara Abreu, o meu pai, Alexandre Abreu e a minha irmã, Marta Abreu. Obrigado pelo vosso amor e apoio incondicional. Sem vocês, não seria o homem que sou hoje e não estaria neste momento a apresentar esta dissertação.

Uma palavra de apreço a todos os amigos que me acompanharam e que fizeram destes anos os melhores da minha vida: Ana Pimentel, Miguel Marques, João Jacinto, João Alcântara, Mariana Ressurreição, Cátia Miguel, Beatriz Vivar, Margarida Beiral, Catarina Paiva, Mafalda Rodrigues e muitos outros. Embora todos sejam importantes para mim, não consigo deixar de destacar quatro pessoas por serem, neste momento, família. João Simão, Frederico Romero, Lourenço Cruz e Pedro Sequeira, muito obrigado por estarem sempre ao meu lado. Para sempre vos estarei gratos.

Por fim, a minha profunda gratidão vai para a minha namorada, Ana Lopes da Costa, por ser, indubitavelmente, a pessoa mais paciente, carinhosa e fantástica que conheço.

Abstract

Aeration is the most energy demanding process in wastewater treatment plants, thus the optimisation of its efficiency has been identified as one of the most crucial endeavours in the field of wastewater engineering. Mathematical modelling of oxygen transfer is a possible solution to this problem, since it enables the comprehension of the underlying physical phenomena involved in this complex process. Although bubble size distribution (BSD) has been pinpointed as one of the key factors in the estimation of oxygen transfer, most state-of-the-art modelling methodologies fail to consider the impact of this parameter. This thesis aims to fill the knowledge gap associated with the influence of BSD on oxygen transfer. To achieve this, a mathematical model that predicts BSD dynamics was developed. The model is based on the population balance modelling (PBM) framework and on a coalescence model. This strategy was applied to a lab scale bubble column to assess its predictive capability. Results show that the model developed is able to accurately predict experimental observations, proving that it can be a valuable tool in estimating BSD dynamics. Therefore, this work is a first step towards the refinement of current oxygen transfer models and, as such, it paves the way for the reduction of energy consumption in wastewater treatment plants.

Keywords

Aeration; Coalescence; Energy efficiency; Oxygen transfer; Wastewater treatment

Resumo

O arejamento é o processo que consome mais energia nas estações de tratamento de águas residuais, pelo que a otimização da sua eficiência é identificada como um dos principais desafios em engenharia ambiental. A modelação matemática da transferência de oxigénio é uma possível solução para este problema, visto que permite a compreensão dos fenómenos físicos envolvidos neste processo. Embora a distribuição do diâmetro das bolhas (DDB) seja um dos fatores chave na determinação da transferência de oxigénio, a maioria dos métodos de modelação não têm em conta o seu impacto. Por este motivo, esta dissertação visa compreender a influência da DDB na transferência de oxigénio. Para atingir este objetivo, foi desenvolvido um modelo matemático capaz de prever a dinâmica da DDB. O modelo baseia-se na teoria de modelação de balanços populacionais e num modelo do fenómeno de coalescência. Esta estratégia foi aplicada a uma coluna de bolhas de tamanho laboratorial, de modo a avaliar a sua capacidade de prever a DDB. Os resultados demonstram que o modelo desenvolvido é capaz de prever os resultados experimentais eficazmente, comprovando o valor do mesmo na descrição da DDB. Em suma, o trabalho desenvolvido constitui um primeiro passo na otimização dos atuais modelos de transferência de oxigénio e abre caminho para a redução do consumo de energia nas estações de tratamento de águas residuais.

Palavras Chave

Arejamento; Coalescência; Eficiência energética; Transferência de oxigénio; Tratamento de águas residuais

Contents

List of Figures

List of Tables

Acronyms

AS	Activated sludge
BSD	Bubble size distribution
CFD	Computational fluid dynamics
CW	Clean water
DO	Dissolved oxygen
FPT	Fixed pivot technique
ODE	Ordinary differential equation
OTR	Oxygen transfer rate
PBM	Population balance modelling
PBME	Population balance modelling equation
SM	Solution method
SSE	Sum of squared errors
TIS	Tank-in-series
XG	Xanthan gum

1

Introduction

Contents

1.1 Background and motivation

Water is an essential resource for human life, ecosystems, and the industry. In many locations, the amount of available fresh water to fulfil human needs has become insufficient. Therefore, its treatment and potential reuse is of the utmost importance. To accomplish this objective, wastewater engineering is an indispensable field. One of the most commonly used operations in a conventional wastewater treatment scheme is the activated sludge (AS) process. This step is key, as it removes suspended solids, biodegradable organic matter, and nutrients from the treated stream.

Numerous improvements in wastewater engineering have been registered in recent years, yet there are still many obstacles to overcome. Among them, the high energy usage of aeration is to be highlighted. This technology is an important piece of conventional wastewater treatment because it is an integral part of an AS process. Decreasing energy consumption is essential to mitigate the environmental impact and increase the cost-efectiveness of wastewater treatment plants. Hence, the optimisation of aeration efficiency in wastewater treatment has been identified as one of the most crucial endeavours in the quest for advanced wastewater treatment.

This thesis aims to provide meaningful insight into the aeration process, namely the impact of bubble size distribution (BSD) on oxygen transfer, so that aeration efficiency can be improved. With this goal in mind, an extensive literature review was performed to fully understand the problem in hand and to pinpoint the current knowledge gaps on this topic. Once these knowledge gaps were identified, a novel mathematical approach was developed to comprehend and describe the problem. The conceptualisation of this new strategy led to the understanding of underlying physical mechanisms involved in oxygen transfer, thus deepening the current knowledge of this topic. In addition, the model was applied to the system studied by Amaral et al. (2018) and proved to be an useful tool in predicting BSD dynamics. Since this concept has been identified as a key factor in oxygen transfer, this model can be a stepping stone for other models that attempt to refine aeration efficiency.

1.2 Objectives

This dissertation aims to continue the work of Amaral et al. (2018), which focused on studying the impact of BSD on oxygen transfer. The primary objective is the development of a model that predicts the BSD dynamics observed by Amaral et al. (2018). The secondary objective is the clarification of the mathematical and physical background associated with BSD.

1.3 Dissertation outline

The dissertation is divided into five chapters: “Introduction”, “Literature review”, “Model development”, “Results and discussion”, and “Conclusions and future perspectives”.

In Chapter 1, the background and motivation of this thesis are presented. After, the main objectives are described and the structure of the dissertation outlined.

In Chapter 2, a literature review was performed to identify the main knowledge gaps regarding aeration efficiency. The aim is to fully comprehend the state-of-the-art oxygen transfer modelling strategies and their main limitations. To understand the aeration process in wastewater treatment, an overview of the essential concepts of this scientific field is given. Furthermore, the theory of gas-liquid mass transfer is thoroughly described, since it is fundamental for the mentioned process.

In Chapter 3, the modelling exercise is explained in detail. This chapter is the core of this thesis as the methodology followed to develop the model is delineated. Firstly, the system studied by Amaral et al. (2018) and the experimental methodology followed by this author are detailed. Secondly, the mathematical framework used to describe BSD is explained. Thirdly, the model used to predict BSD dynamics is formulated. Moreover, all assumptions and considerations made during the modelling exercise are presented. Finally, the model inputs as well as the calibration and validation processes are described.

In Chapter 4, the model is applied to the system studied by Amaral et al. (2018) and validated. The focus is on the performance of the model, which is analysed and thoroughly discussed.

In Chapter 5, the conclusions of this thesis are summarised and future research directions identified.

2

Literature Review

Contents

2.1 Wastewater treatment

Water is an essential resource for the life of all beings on Earth. Concurrently, it is also the most used liquid resource in human activities (Chaplin, 2001). Although water is abundant on Earth, humans strongly depend on a specific type of water: fresh water. The dependence is mostly related to biological needs, such as drinking, and to human activities, such as agriculture, industry, and cleaning. Moreover, in recent times, the improving standard of living is also contributing a lot to this dependency, since many leisure activities rely on fresh water and a high standard of living is associated with a high requirement of fresh water (Maitland, 1990).

When analysing the amount of global water (Figure 2.1), it is possible to understand that fresh water is rather scarce. This condition will tend to worsen throughout the years, since the Earth's population will keep rising and the amount of available fresh water is limited (Maitland, 1990). Furthermore, once fresh water is used by an organism or in a human activity, it usually becomes polluted, which makes it unusable and a hazard to public health and the environment. Bearing all this in mind, one can infer that the treatment and potential reuse of the water generated by living beings' natural processes and human activities are of the utmost importance (Jenkins and Wanner, 2014; Metcalf and Eddy, 2003). As such, the development of a specific scientific field to tackle the problems that arise from water usage is fundamental.

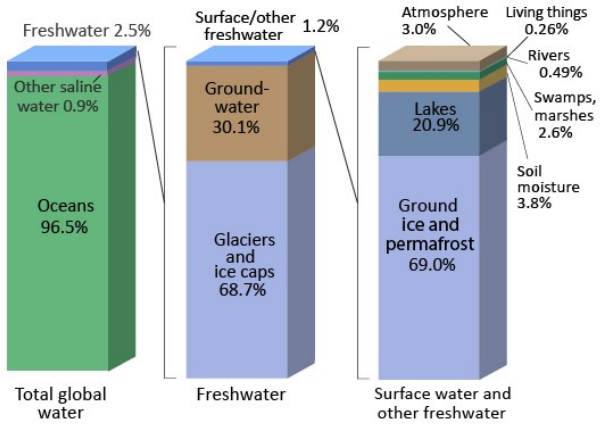

Figure 2.1: Percentage and distribution of fresh water on Earth. Adapted from Gleick (1993).

The scientific field devoted to solve the problems described above is called wastewater engineering. The goal of this branch of environmental engineering is to research, develop, and implement tools to treat wastewater, which is a combination of the liquid or water-carried wastes that are removed from domestic, industrial, and commercial establishments that may contain stormwater, groundwater or surface water. Due to its origin, wastewater is composed of many different chemicals, organic matter, pathogens

and physical particles which make its treatment challenging. Therefore, wastewater engineering focuses on solving the issues related to the treatment and reuse of wastewater. Its ultimate objective is the protection of public health, respecting the political, social, and economic concerns as well as the environment (Metcalf and Eddy, 2003).

The treatment process applied to wastewater can be divided into four steps: (1) to identify characteristics of the untreated wastewater; (2) to identify treatment objectives; (3) to develop a process layout able to fulfil the defined objectives; and (4) integrating sustainability concepts to decrease energy consumption and enable water reuse (Mihelcic and Zimmerman, 2010). These four steps translate into a conventional wastewater four-stage treatment (figure 2.2). The first stage is called pre-treatment and its main objective is the removal of physical particles and oils (this avoids damage to the equipment used and the inhibition of biological processes). The second stage is the primary treatment which removes solids through quiescent, gravity settling. The secondary treatment with nutrient removal (third stage) removes the suspended solids, biodegradable organic matter, and nutrients - Nitrogen (N), Phosphorus (P) - present in the wastewater (see section 2.2.1). Finally, the ultimate stage is the tertiary treatment which aims to remove residual suspended solids and nutrients (if needed) as well as the disinfection of the wastewater (Metcalf and Eddy, 2003; Mihelcic and Zimmerman, 2010).

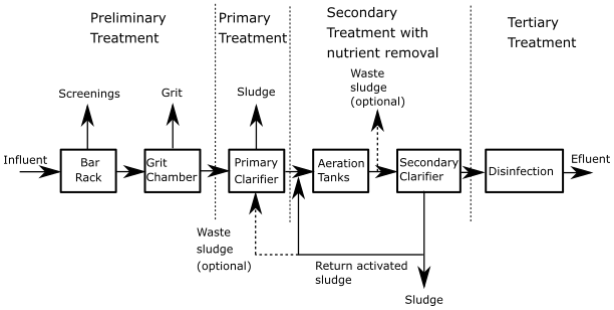

Figure 2.2: Simplified flow diagram of the conventional four-stage wastewater treatment. Adapted from Metcalf and Eddy (2003).

Although the conventional approach is very effective in removing pollutants and pathogens, there are still many concerns regarding this process. Among them, the high energy consumption is to be highlighted, since the amount of electricity used for wastewater treatment accounts for a large portion of electricity use worldwide (e.g. case of the United States (Mihelcic and Zimmerman, 2010), and Germany (Sommer et al., 2017)). Many authors have been focusing on this issue and concluded that aeration is the most energy demanding process in wastewater treatment (Fayolle et al., 2007; Jiang et al., 2017; Rosso and Stenstrom, 2006a).

2.2 Aeration in wastewater treatment

Aeration can be described as a process which consists on the addition of air into a liquid medium. This process is intimately related with wastewater treatment since most biological processes require the presence of oxygen. In this section, the importance of aeration in wastewater treatment, especially in activated sludge (AS) processes, is showcased, as well as the characteristics of the aeration systems. Finally, the problems related to aeration are pinpointed and a possible solution identified.

2.2.1 Importance of aeration

The third stage of a conventional treatment scheme includes a biological treatment: a key activity to the overall wastewater treatment process. One of the most commonly used biological processes in wastewater treatment is the AS process (Jenkins and Wanner, 2014), which has five functions: (1) suspension of a flocculent slurry of microorganisms via mixing and/or aeration; (2) transformation of dissolved and particulate biodegradable constituents (organic matter) into acceptable end products and removal of nutrients (such as N and P) using microorganisms, principally bacteria (figure 2.3); (3) liquid-solids separation to reduce the total suspended solids concentration; (4) return of solids from the liquid-solids separation zone to the suspended growth-treatment reactor; and (5) wasting of excess sludge to maintain the desired mass (Jenkins and Wanner, 2014; Metcalf and Eddy, 2003). The simplified flow diagram of the AS process is depicted in figure 2.2 in the part denoted by secondary treatment with nutrient removal. Despite the importance of all the functions in the global AS process, this section focuses solely on the second one, since it is the only one directly associated with aeration.

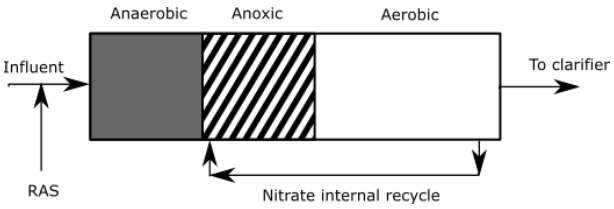

Figure 2.3: Layout of the bioreactor in which the biological treatment involved in the second step of the AS process takes place. Adapted from Jenkins and Wanner (2014).

Of the many possible configurations for the AS process, the one shown in figure 2.3 is the most common. There are three sections in which the influent (that comes from primary treatment) and the recycled AS (recirculated to the reactor from the liquid-solids separation zone) must pass. Due to the different environmental conditions in each section, there are significant differences in both the microorganisms and the biological reactions involved. To comprehend this step, a brief overview of the biological reactions and environmental characteristics is given.

The first section is anaerobic, which means that there is neither dissolved oxygen (DO) nor oxidised nitrogen. In these conditions, only a small array of microorganisms can grow and perform their activities. In the AS process, the microorganisms that thrive in anaerobic conditions are the phosphorous storing ones. The second section is anoxic, i.e. there is absence of DO but nitrates are present. In this case, two biological processes take place. One of them is denitrification, which is defined as the conversion of nitrate nitrogen into nitrogen gas. The other is carried out by the phosphorous storing microorganisms which grow in anaerobic conditions. In anoxic conditions, these microorganisms change their metabolism leading to the uptake and storage of soluble phosphorous (Peng et al., 2006). Lastly, the third section is aerobic (presence of both DO and nitrates), where three important processes occur: nitrification, oxidation of the organic matter into simple end products, and uptake of inorganic phosphorous. The first one - nitrification - is the biological oxidation of ammonia to nitrite and then to the nitrate form. The second process is the transformation of organic matter into carbon dioxide, water, and new cells in the presence of oxygen, ammonia, and phosphate by microorganisms, principally bacteria (equation 2.1). The last one is the same process described in the anoxic section, which can also occur in aerobic conditions (Surampalli et al., 1997).

$$\mathbf{v}_1(organic\,matter) + \mathbf{v}_2\mathbf{O}_2 + \mathbf{v}_3\mathbf{NH}_3 + \mathbf{v}_4\mathbf{PO}_4^{3-} \overset{microorganisms}{\rightarrow} \mathbf{v}_5(new\,cells) + \mathbf{v}_6\mathbf{CO}_2 + \mathbf{v}_7\mathbf{H}_2\mathbf{O} \quad (2.1)$$

Considering all the information regarding the biological reactions and microorganisms involved, one can conclude that the combination of all these processes accomplishes the removal of organic matter, N, and P. The removal of organic matter takes place in the aerobic region and the process is described by equation (2.1). The removal of N occurs due to the combination of the nitrification and denitrification steps. The nitrifying microorganisms transform the ammonia into nitrates that are recycled to the anoxic zone (see figure 2.3). In this zone, the denitrifying microorganisms transform the nitrates into nitrogen gas leading to its removal from the wastewater. Finally, the removal of P is associated with both the anaerobic (growth of phosphorous storing microorganisms) and aerobic zones (uptake of soluble phosphorous by the microorganisms) (Surampalli et al., 1997).

There are several biological components and molecules involved in the process described. One of the most important is oxygen because its presence or absence strongly affects cell behaviour and metabolism. In the case of aerobic processes, oxygen is the principal electron acceptor playing a crucial role in bacterial metabolisms (Teixeira and Fonseca, 2006). Therefore, aeration is indispensable to the success of AS processes.

Another important role related to aeration is mixing. The two processes often go hand in hand since the movement of gas bubbles causes a motion in the liquid as well. Nonetheless, this action is not enough to allow the spreading of the DO throughout the reactor, thus the use of additional mixing strategies is needed (see section 2.2.3). It should be noted that the presence of DO in all parts of the bioreactor leads to the covering of the culture's oxygen demand in any point of the tank, thus increasing process effectiveness (Amaral et al., 2018).

2.2.2 Types of aeration

In wastewater treatment, aeration can be carried out using many different strategies. To choose the best approach, there are several conditions that have to be analysed, such as the function of the aeration system, type and geometry of the reactor, and installation and operation costs. Despite the existence of several alternatives, these can be grouped into three main categories: diffused-air systems, mechanical aeration, and high-purity oxygen systems (Metcalf and Eddy, 2003). For AS processes, which are the most common biological treatment processes in the world for both municipal and industrial wastewater (Jenkins and Wanner, 2014), diffusers and mechanical aerators are commonly used (Teixeira and Fonseca, 2006).

Diffusers introduce compressed air in the form of bubbles using a submerged dispersion system (Figure 2.4 a)). According to the physical characteristics of the equipment, diffusers are divided into three types: porous or fine-pore diffusers, nonporous diffusers, and other diffusion devices (jet aerators, aspirating aerators, and U-tube aerators) (Metcalf and Eddy, 2003). The fine-pore diffusers are installed on the bottom of the reactor and are often full-floor coverage, i.e. they occupy the entire bottom surface of the reactor. The bubbles generated by this system are fine, which means that they have less than 5 mm diameter (Rosso and Stenstrom, 2006b). These two characteristics allow for a uniform spread of DO and a large bubble contact time, which increases the oxygen transfer efficiency (Jenkins and Wanner, 2014). Nonporous diffusers produce coarse bubbles, which have a diameter that ranges from 6 mm to 50 mm (Rosso and Stenstrom, 2006b), and are often mounted to tank walls or in wide bands, spiral roll, cross roll, ridge and furrow (Jenkins and Wanner, 2014). Even though this system provides excellent mixing, it has a lower aeration efficiency compared to the fine-bubble alternative because the bubble retention time is smaller (Jenkins and Wanner, 2014; Metcalf and Eddy, 2003). Jets and aspirating aerators can be combined to produce fine bubbles and are suited for deep tanks ($>$8 m) (Metcalf and Eddy, 2003).

Mechanical aerators are divided into two groups: aerators with vertical axis (Figure 2.4 b) and c)) and aerators with horizontal axis. Both groups are then subdivided into surface and submerged aerators.

For the case of surface aerators, atmospheric oxygen is entrained and mixed with the liquid. In the submerged aerators case, atmospheric oxygen is entrained to the liquid and, for some types, oxygen is introduced in the tank bottom. In both cases, the pumping or agitating action is responsible for the mix of the basin contents. This type of aeration is not used in AS processes except in low-speed turbine aerators. This system consists of a large-diameter turbine that exposes droplets of liquid to the atmosphere (Metcalf and Eddy, 2003).

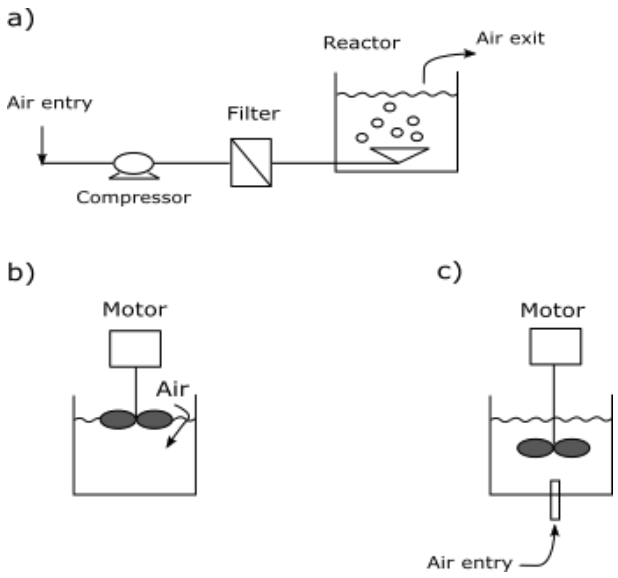

Figure 2.4: Types of aeration of AS processes. a) - Diffusers, b) -Surface mechanical aerator, c) – Submerged mechanical aerator with introduction of air. Adapted from Teixeira and Fonseca (2006).

2.2.3 Challenges of aeration

Aeration is reported as the operation that accounts for most of the energy consumption in wastewater treatment plants, representing up to 70 per cent of the total energy expenditure of the plant (Fayolle et al., 2007). As previously discussed (section 2.2.1), aeration plays a vital role in AS processes. Such operation provides the oxygen needed for the occurrence of cell metabolism and contributes to the mixing of the tank content. Due to its crucial role in wastewater treatment, this process cannot be discarded when tackling the problem of energy consumption. Thus, aeration must be further studied so that operation costs and energy usage can be decreased (Fayolle et al., 2007; Karpinska and Bridgeman, 2016).

Initially, the answer to reduce the high energy consumption was the installation of fine-pore diffusers, as these have higher efficiencies per energy unit consumed (Rosso and Stenstrom, 2006b). Due to its energy efficiency characteristics, even the replacement of surface aeration systems by porous diffusers in full floor configuration was encouraged since it was an easy way to decrease energy consumption

(Karpinska and Bridgeman, 2016). This approach made the fine-pore diffusers the most common aeration technology in wastewater treatment in developed countries (Rosso and Stenstrom, 2006b). Despite reducing energy costs by 50 per cent when compared with coarse-bubble diffusers (Mihelcic and Zimmerman, 2010), this option did not solve the problem of high energy usage. Therefore, further review of the present approaches is required to improve the development, troubleshooting and management of aeration systems (Karpinska and Bridgeman, 2016).

Amaral et al. (2017) argues that, to satisfy the demand for better and improved approaches, mathematical modelling of the entire aeration system is needed. The development of aeration models will be essential in view of the design, optimisation, and control of wastewater treatment plants. Nowadays, the consensus among researchers is that aeration models are less refined than state-of-the-art biokinetic and settling models. The inherent complexity of the aeration systems used in present models is considered to be the reason (Amaral et al., 2017). Therefore, the authors believe that research efforts should point towards facing the complexity present in the aeration system (blowers, air piping, diffusers) and the oxygen transfer from the bubbles to the bulk liquid. This position is supported by their work, which identified several problems and limitations on all parts of the modelling of aeration system and on the modelling of mass transfer. Although research efforts are achieving some progress, there are still many issues that must be addressed. Nonetheless, it is possible to notice that these efforts are resulting in improved predictions of DO profiles and in lower energy consumption. Consequently, it is possible to argue that mathematical modelling can be used to optimise the current aeration models (Amaral et al., 2017).

Even though mathematical modelling has been identified as a possible solution, the task remains challenging and complex (Amaral et al., 2017). The aeration system is divided into two different parts: air generation and distribution and oxygen transfer. Despite being separated, a link between the two exist since oxygen transfer is influenced by the number and arrangement of diffusers and mixing conditions. In addition, inside the air generation and distribution system there are interactions between pieces of equipment, which can impact the efficiency of the blower. Bearing this in mind, it is possible to deduce that mathematical modelling of the entire aeration system is extremely difficult (Amaral et al., 2017). As such, current research is focusing on detailing aeration submodels, that is, studying parts of this system instead of studying the whole at once. Such an approach results in an increased understanding of the underlying mechanisms and the improvement of the predictive capabilities of the models. Although it raises a challenge when connecting the submodels, this path is seen as the most viable alternative to tackle this problem (Amaral et al., 2017).

Due to the complexity of the aeration system, this thesis only focuses on the modelling of oxygen transfer.

2.3 Fundamentals of oxygen transfer mathematical modelling

Aeration is commonly done in AS processes by introducing compressed air at the bottom of the tank with fine-pore diffusers since this is the most energy efficient method (see section 2.2.3). This leads to the dispersal of the gas, in the form of bubbles, throughout the liquid. The oxygen that is essential to cell metabolism is inside the bubbles and, to be utilised by the cells, needs to be solubilised. The oxygen transference from the bubbles to the bulk is described by the gas-liquid mass transfer theory. Consequently, the first step towards aeration modelling optimisation is the understanding of the physical phenomena behind it.

2.3.1 Theoretical basis

In this section, the equation used to describe mass transfer as well as the most accepted theory to describe gas-liquid mass transfer are presented and thoroughly explained. The section ends with the introduction to the concept of volumetric mass transfer coefficient (K_La).

2.3.1.A Fick's First Law of diffusion

Mass transfer is the movement of molecules from one homogeneous phase to another. This phenomenon only takes place if a pressure or concentration gradient is present. When the gradient exists, the molecules move spontaneously from the higher concentration to the lower concentration zone. The movement described is named 'diffusion process'. The gradient involved in mass transfer depends on the phases that are present. A partial pressure gradient is related to gaseous components and a concentration gradient to liquids and solids. Mass transfer will stop once equilibrium conditions prevail, which happens when the gradient ceases to exist (Metcalf and Eddy, 2003; Teixeira and Fonseca, 2006).

When a concentration or pressure gradient exists, component transport through diffusion between phases is described by Fick's First Law of diffusion:

$$r = -\mathbf{D}_m \times \frac{dC}{dx} \tag{2.2}$$

Equation (2.2) states that the amount of substance, in steady state conditions, transported by diffusion per units of time and area is proportional to the concentration gradient. The factor of proportionality (D_m) is denominated 'diffusion coefficient'. The minus sign reflects the fact that molecules move in an

opposite direction to the concentration gradient (Teixeira and Fonseca, 2006). It should be noted that the amount of substance can either be expressed in terms of mass or substance amount (mole). The latter is often used when studying gas-liquid mass transfer since the gas is measured in mole.

Equation (2.2) is the cornerstone of all mass transfer studies and it is applicable when studying all types of mass transfer, regardless of the phases involved. However, depending on the flow regime, Fick's First Law of diffusion must be adapted. This adaptation consists on changing the diffusion coefficient to a turbulent coefficient (in case of turbulent regime) or to a coefficient of dispersion (in case of transitional regime, i.e. the regime between laminar and turbulent) (Metcalf and Eddy, 2003).

2.3.1.B The Two-Film Theory

When a bubble of gas is inside a liquid, an interface is present around the bubble. This interface, denominated 'gas-liquid interface', has characteristics that are neither easily observed nor explained. Nonetheless, numerous theories have been developed throughout the years with the purpose of understanding the details of gas-liquid mass transfer. The more complex theories are the ones proposed by Higbie and Danckwerts, because they take into consideration more physical phenomena involved in this type of mass transfer. Yet, the most accepted one is the Two-film theory which is more simplistic. This acceptance is supported by the fact that, in most cases, the results achieved by this theory are the same as those obtained by the more complex theories (roughly 95 per cent of the cases). In addition, even in circumstances where it appears to fail, it is unclear whether other theories are better. Due to these observations, the Two-film theory is the one that is used to explain gas-liquid mass transfer (Metcalf and Eddy, 2003).

The Two-film theory states that, when a bubble is inside a liquid, the gas-liquid interface is constituted of two films: the liquid film and the gaseous film. Therefore, the system is composed by four entities which are the bulk gas, the gas film, the liquid film, and the bulk liquid. The theory considers two possible scenarios for gas-liquid mass transfer. The gas is either going from the gas phase to the liquid phase (absorption phenomenon) or going from the liquid phase to the gas phase (desorption phenomenon). A visual scheme of the system and the two scenarios considered are displayed in Figure 2.5 a) and Figure 2.5 b).

According to this theory, all resistance to mass transfer is provided by these two films. Nevertheless, this conclusion is based on an assumption which states that the concentration in the liquid phase and the partial pressure in the gas phase are uniform. In practice, the assumption is justified if the system operates under perfect mixing conditions (Metcalf and Eddy, 2003). According to some authors (Amaral

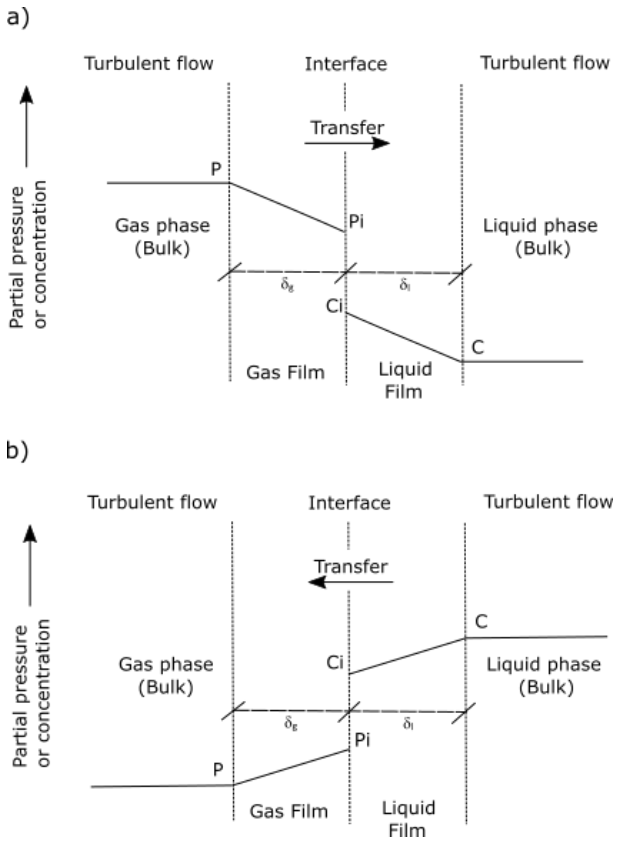

Figure 2.5: Absorption (a)) and desorption (b)) phenomena according to the Two-film theory. Adapted from Metcalf and Eddy (2003).

et al., 2017; Rehman et al., 2017), this cannot be assured (see section 2.5.1). Despite concerns related to the reliability of this consideration, the studies developed in this scientific field mostly assume that this ideal situation portrays the phenomena observed in the operations that take place in bioreactors.

Under steady-state conditions, the rate of mass transfer of a gas through the gas film must be equal to the transfer rate through the liquid film. Using Fick's First Law of diffusion and assuming perfect mixing conditions, the mass flux for each phase for absorption is defined by equation (2.3).

$$r = \mathbf{k}_G \times (\mathbf{P}_G - \mathbf{P}_i) = \mathbf{k}_L \times (\mathbf{C}_i - \mathbf{C}_L) \tag{2.3}$$

In equation (2.3), r denotes the rate of mass transferred per unit area per unit time, and P_G and P_i designate the partial pressures of the constituent in the bulk of the gas phase and at the interface in equilibrium with C_i, respectively. Moreover, C_i and C_L represent the concentration of the constituent at the interface in equilibrium with P_i and in the bulk liquid phase, respectively. It should be noted that the usual diffusion coefficient is replaced by the coefficient k_L for the liquid phase and by the coefficient k_G for

the gas phase. These coefficients represent the resistance of the liquid film and gas films, respectively. Additionally, the resistance is only considered to exist in the films since the assumption of perfect mixing is assumed.

With equation (2.3) it is possible to calculate the mass flux for each phase for absorption by knowing the coefficients k_L and k_G. Still, these coefficients are not easily measured at the interface (Metcalf and Eddy, 2003). Due to this impracticality, the coefficients used are overall mass transfer coefficients. If it is considered that the critical resistance to mass transfer is on the liquid side, the overall coefficient used is K_L. Conversely, if the critical resistance is found on the gas side, the overall coefficient used is K_G. To understand which of the films controls mass transfer, a relation between the two overall mass transfer coefficients must be established. The following steps show the deduction of this relationship.

If resistance to mass transfer is controlled by the liquid film, the rate of mass transfer is described by equation (2.4).

$$r = \mathbf{K}_L \times (\mathbf{C}_S - \mathbf{C}_L) \tag{2.4}$$

The gradient of concentrations considered in equation (2.4) is between the component's concentration at the interface in equilibrium with the component's partial pressure in the bulk gas phase and the component's concentration in the bulk liquid phase. Due to the assumption that all the resistance to mass transfer is on the liquid side, Henry's Law can be applied to the interface, resulting in the relationships presented by equations (2.5) and (2.6).

$$\mathbf{P}_G = H \times \mathbf{C}_S \tag{2.5}$$

$$\mathbf{P}_i = H \times \mathbf{C}_i \tag{2.6}$$

Furthermore, the overall driving force can be written as seen in equation (2.7).

$$(\mathbf{C}_S - \mathbf{C}_L) = (\mathbf{C}_S - \mathbf{C}_i) + (\mathbf{C}_i - \mathbf{C}_L) \tag{2.7}$$

Starting from equation (2.7) and using equations (2.3) to (2.6) it is possible to deduce equation (2.8).

$$\frac{1}{\mathbf{K}_L} = \frac{1}{\mathbf{k}_L} + \frac{1}{H\mathbf{k}_G} \tag{2.8}$$

Following the same rationale presented but now considering that the gas side is controlling the resistance to mass transfer, equation (2.9) can be written as:

$$\frac{1}{\mathbf{K}_G} = \frac{1}{\mathbf{k}_G} + \frac{H}{\mathbf{k}_L} \tag{2.9}$$

Finally, using equations (2.8) and (2.9) the relationship between the two overall mass transfer coefficients can be defined – equation (2.10).

$$\frac{1}{\mathbf{K}_L} = \frac{1}{\mathbf{K}_G \times H} \tag{2.10}$$

From equation (2.10) it is easy to conclude that if the value for Henry's constant is high, the liquid side is controlling the resistance to mass transfer since K_L will assume a high value as well. This conclusion is of the utmost importance, because it enables a prediction of which side is controlling the resistance to mass transfer only by knowing the value of the Henry's constant of a gas. For the case of slightly soluble gases, like oxygen and carbon dioxide, the liquid side is often responsible for the resistance to mass transfer (Metcalf and Eddy, 2003; Teixeira and Fonseca, 2006).

2.3.1.C Definition of K_La

When studying aeration in AS processes, the oxygen transfer rate (OTR) is often described per unit of volume per unit of time, instead of per unit of area per unit of time. Besides that, the concentration of oxygen in the liquid phase is considered to be a function of time. Due to these differences, equation (2.4) is rewritten as equation (2.11).

$$OTR = \mathbf{K}_L a \times (D\mathbf{O}_{sat} - DO) \tag{2.11}$$

In equation (2.11), the term *DO* refers to the concentration of oxygen in the liquid phase at time *t* and DO_{sat} to the concentration in equilibrium with the gas, as given by Henry's Law. The term K_La is the product of two different parameters. The first one is the overall liquid mass transfer coefficient, K_L, and the second is the interfacial area available for mass transfer per unit volume, *a*. The latter is obtained

by dividing the area through which oxygen is transferred by the volume in which oxygen concentration is increasing. This coefficient arises from the change of unit of area to unit of volume in the rate of mass transfer. Finally, it is important to note that the two-film theory is used in order to write equation (2.11), since it was considered that all the resistance to mass transfer is on the liquid side. Hence, the use of the term K_L (Metcalf and Eddy, 2003).

Due to the importance of the K_La in oxygen transfer, there is a need to measure it accurately. In section 2.3.2, the current methods employed in the measurement of this parameter are described and discussed.

2.3.2 Measurement of K_La

The determination of the K_La is essential to predict the oxygen transfer rate. Even though it is a product of two different parameters, it is often obtained experimentally in a lumped form, due to the difficulties in measuring the two parameters separately (Teixeira and Fonseca, 2006). However, even when measured as a product, it is problematic to accurately determine this variable, since it changes with several conditions (Amaral et al., 2017). Therefore, the method to measure the operational K_La involves using a standard value and correction factors. These factors estimate the impact of the operating conditions on the standard K_La, adjusting it to each specific case. Since this coefficient is sensitive to many conditions, there are different correction factors, each one accounting for a different effect (Metcalf and Eddy, 2003).

The standard value of K_La is defined as the value measured in tap water at 20 ℃, 1 atm, zero salinity and zero DO. The most accepted method to determine it is the American Society of Civil Engineers method (American Society of Civil Engineers, 1983). After the assessment of this value, the differences between standard conditions and operating conditions must be evaluated to choose the correction factors that need to be used. There are three correction factors: the α-factor, the θ-factor, and the F factor (Metcalf and Eddy, 2003).

The α-factor is one of the most important and used correction factors. It measures the effects of mixing intensity, tank geometry, and wastewater characteristics on the standard K_La value, which are known to decisively affect the overall oxygen transfer performance of the aeration system (Jiang et al., 2017). Its definition can be found in equation (2.12).

$$\alpha = \frac{\mathbf{K}_L a\ (wastewater)}{\mathbf{K}_L a\ (tap\, water)} \tag{2.12}$$

As seen in equation (2.12), the α-factor is the ratio between the K_La of the process and the standard K_La. Due to the importance of this factor in aeration, several studies have been conducted to determine its value. Even though no significant conclusions could be drawn due to its high variation with operating conditions, values ranging between 0.3 and 1.2 have been reported in the literature (Metcalf and Eddy, 2003).

The θ-factor corrects the effect of temperature on oxygen transfer which is described by equation (2.13).

$$\mathbf{K}_L\mathbf{a}_{(T)} = \mathbf{K}_L\mathbf{a}_{(20^\circ C)} \times \theta^{(T-20)} \tag{2.13}$$

Once again there are differences in the values reported in the literature. Despite this, the discrepancy between the values is significantly lower than the one documented for the α-factor. Consequently, the use of 1.024 for the θ-factor is accepted (Metcalf and Eddy, 2003).

Finally, another factor used is the F factor, which considers the effects of both external and internal fouling on diffused aerators. The values of this factor range between 0.65 and 0.9 (Metcalf and Eddy, 2003).

In equation (2.14) the full expression to calculate the process K_La involving all the correction factors is shown. When an effect on the standard K_La is discarded, the corresponding correction factor assumes the value 1.

$$Actual\ \mathbf{K}_La = \alpha \times \theta^{(T-20)} \times F \times Standard\ \mathbf{K}_La \tag{2.14}$$

There is one more effect that has not been accounted for, which is the influence of water constituents on the system OTR. There are some substances such as salts, particulates, and surface-active agents that affect the oxygen solubility, and consequently influence the oxygen transfer. The correction factor that describes this effect is known as the β-factor and it is defined in equation (2.15).

$$\beta = \frac{\mathbf{C}_P\ (wastewater)}{\mathbf{C}_P\ (clean\ water)} \tag{2.15}$$

As seen in equation (2.15), the β-factor is the ratio between the concentration of the constituents in wastewater and the concentration of the constituents in tap water. This factor often ranges from 0.7 to 0.98 and it is relatively easy to predict. The most commonly used value is 0.95 (Metcalf and Eddy, 2003).

Applying all these correction factors to equation (2.11) it is possible to obtain equation (2.16).

$$Actual\ OTR = Actual\ \mathbf{K}_L a \times (\beta \times \mathbf{DO}_s at - \mathbf{DO}) \tag{2.16}$$

Equation (2.16) states that the process oxygen transfer rate, actual OTR, is the standard OTR adjusted with all the correction factors.

2.4 State-of-the-art modelling of oxygen transfer

In this section, the rationale behind the state-of-the-art modelling of oxygen transfer is described. Next, the strategy followed by the current modelling approach is defined and the main bottlenecks pinpointed. The section concludes with the identification of future endeavours.

The study of aeration in AS processes starts with the generic oxygen mass balance described by equation (2.17).

$$Accumulation = Inflow - Outflow + Increase\,due\,to\,absorption - Consumption\,by\,microorganisms \tag{2.17}$$

Considering a generic continuous aerobic operation occurring on a bioreactor, equation (2.17) is transformed into equation (2.18).

$$\frac{dDO}{dt} = \frac{Q}{V} \times D\mathbf{O}_{in} - \frac{Q}{V} \times D\mathbf{O}_{out} + \mathbf{K}_L a \times (D\mathbf{O}_{sat} - DO) - OUR \tag{2.18}$$

In equation (2.18), the left-hand side represents the rate of accumulation of oxygen within the system boundary. The right-hand side is composed by four different expressions. The first one describes the rate of flow of oxygen into the system boundary, whereas the second one the rate of flow of oxygen out of the system boundary. Due to the presence of cells and the introduction of air by the aeration system, two more terms are needed to complete the oxygen mass balance. The third one describes the amount of oxygen absorbed through the system boundary, known as OTR, and the forth one the amount of oxygen consumed by the cells (OUR) (Metcalf and Eddy, 2003; Teixeira and Fonseca, 2006).

When steady-state conditions are attained, and if the amount of DO that enters and leaves the system in the liquid streams is much lower than the amount supplied by the aeration system, equation (2.18) is simplified to equation (2.19).

$$\mathbf{K}_L a \times (D\mathbf{O}_{sat} - DO) = \mathbf{q}_{\mathbf{O}_2} \times X \tag{2.19}$$

The left-hand side of equation (2.19) is the OTR and the right-hand side is the oxygen uptake rate. As previously stated, the former measures the amount of oxygen that enters the system by the absorption phenomenon and the latter the amount of oxygen consumed by the cells, which varies with the type of microorganisms present. Knowing the microorganisms specific oxygen consumption rate, q_{O_2}, and its concentration in the liquid, X, it is possible to calculate the critical OTR. The critical OTR is the minimum value for which oxygen is not the limiting factor of cell growth, which is of the utmost importance in aerobic processes. Therefore, the aeration system must be able to ensure a slightly higher value than the one calculated by equation (2.19) (Teixeira and Fonseca, 2006). However, significantly higher or lower values can have devastating consequences for the cells, because the DO level strongly affects their metabolism. Moreover, DO is one of the principal parameters responsible for maintaining optimal conditions and controlling effluent quality, thus the need for the process aeration system to be correctly designed and optimised (Pittoors et al., 2014).

As seen in section 2.3.2, the theoretical equation to determine the OTR is equation (2.16) which considers all the possible effects over the standard oxygen transfer rate. State-of-the-art modelling of aeration systems relies on this equation to calculate the OTR of the process, using it to design the aeration system. The strategy followed by the current modelling approach is simple and straightforward (Amaral et al., 2017, 2018): (1) determination of the standard K_La value using the American Society Civil Engineering method (American Society of Civil Engineers, 1983), preferably on the tank that is going to be used on the process to reduce uncertainty (Metcalf and Eddy, 2003); (2) estimation of the α-factor experimentally or by adopting a value reported in the literature. This value is either used as a constant or as a function of the air flow rate; (3) the θ-factor, β-factor, and F factor are also extracted from the literature when needed. The usually utilised values are the ones presented in Metcalf and Eddy (2003); and (4) calculation of the actual OTR by equation (2.16).

Due to the high energy usage of the aeration system, it is easy to conclude that the current aeration modelling of oxygen transfer has much room for improvement (Pittoors et al., 2014). This is not surprising since the method used is too simplistic (Amaral et al., 2017). There are many different hydrodynamic and operating effects involved in oxygen transfer, such as the flow regime (Shah et al., 1982), the presence of surfactants (Jimenez et al., 2014; Rosso and Stenstrom, 2006b), the rheological characteristics of AS (Durán et al., 2016; Ratkovich et al., 2013), the tank shape (Pittoors et al., 2014), the mixing conditions (Deckwer et al., 1974), the number and arrangement of diffusers (Gillot et al., 2005; Terashima et al., 2016), and the water depth (Gillot et al., 2005). Even though all these parameters significantly impact the oxygen transfer, only the α-factor is currently used to account for them (Amaral et al., 2017, 2018). Obviously, this makes this correction factor one of the most uncertain aeration parameters (Karpinska and Bridgeman, 2016), with reports stating that its value fluctuates through daily cycles and seasonal periods (Jiang et al., 2017). Despite this, the use of constant α-factors is still the most common practice

in process design and modelling, which leads to nonoptimal designs(Jiang et al., 2017).

To improve oxygen transfer modelling, many researchers have been focusing on pinpointing the main physical mechanisms affecting this complex process. Sommer and co-workers identified bubble size distribution (BSD) as one of the key factors affecting oxygen transfer, since it affects both the gas holdup and the bubble size, which have effect on both K_L and a (Sommer et al., 2017). Rehman *et al.* challenged the assumption of completely mixed conditions in bioreactors, defending that there are differences in the DO profile throughout the reactor, which has strong implications on the theory behind oxygen transfer (Rehman et al., 2017), due to the assumption of the two-film theory. Therefore, the comprehension of BSD impact on oxygen transfer and the understanding of the implications of a variable DO profile appear to be the next steps in refining oxygen transfer modelling.

2.5 Towards advanced oxygen transfer modelling

The conjecture stated at the end of section 2.4 was confirmed by the works of Rehman *et al.* (Rehman et al., 2017) and Amaral *et al.* (Amaral et al., 2018). The first work concluded that the well-mixed conditions cannot be assured, thus questioning the current oxygen transfer modelling approaches. The second work determined that the BSD dynamics strongly affect oxygen transfer. Moreover, this research also increased the understanding of the underlying physical mechanisms involved in oxygen transfer because the authors studied K_L and a separately, following the suggestions made by Bouaifi *et al.* (Bouaifi et al., 2001) and Jimenez *et al.* (Jimenez et al., 2014). Due to the importance of these two works on shaping the future of oxygen transfer modelling, they are further described in this section.

2.5.1 Added value of CFD-integrated models

Usually, aeration modelling is supported by a tanks-in-series (TIS) modelling approach, which is a train of virtual completely mixed reactors (Amaral et al., 2017). Due to the well-mixed assumption, this method is unsuitable to evaluate the detailed impact of certain design parameters such as tank geometry, number and type of propellers, and aerator system design on the performance of the biological processes. Therefore, the development of new strategies that consider the spatial variations in substrate and DO in bioreactors is crucial to improve the state-of-the-art oxygen transfer models (Rehman et al., 2017).

With this goal in mind, Rehman and co-workers aimed to further understand the limitations of this hypothesis when trying to accurately describe the oxygenation capacity of the system. The first step was the creation of a computational fluid dynamics (CFD) model since this method takes into consideration the local impact of mixing conditions. Hence, discarding the usual hypothesis of perfectly well-mixed

conditions. The second step was the integration of the CFD model with the current biokinetic and settling models at full scale, something that was still missing in recent studies developed in this area (Rehman et al., 2017). The modelling strategy was experimentally validated and compared with the state-of-the-art modelling approaches so that differences between them could be measured and conclusions be drawn.

From the experimentally validated CFD model obtained by Rehman *et al.*, two important observations could be made. The first one is that both the gas holdup (Figure 2.6(a)) and liquid velocity (Figure 2.6(b)) significantly vary throughout the bioreactor. Regarding the gas holdup, the results show that this parameter varies not only in the direction of bulk flow but also across the width of the reactor. Besides that, it was also possible to detect that the maximum gas holdup occurs after the aerated zone, as shown in Figure 2.6(a). According to the authors, this observation is to be expected since the liquid drags air bubbles, which makes the most oxygenated zone the one adjacent to the area where the compressed air is introduced (Rehman et al., 2017). Regarding liquid velocity, the results showed that in low aerated zones, some regions could be considered as 'dead zones', which are defined by their low mass transfer rates, as seen in Figure 2.6(b). The second observation is that even in the aerated zone, the DO profile varies along the length and width of the reactor (Figure 2.6(c)). Besides that, different sections of the reactor have different levels of heterogeneity in DO (Figure 2.6(c)). These two observations question the state-of-the-art modelling strategy, since none of these effects are accounted for in TIS modelling (the variation of DO concentration along the width of the reactor, the dead zones, and the heterogeneity of DO concentrations along the reactor are ignored because uniform mixing is assumed).

To support the conclusions drawn from the CFD model, Rehman and co-workers introduced a new concept denominated 'concentration distribution plots' and developed a TIS model to describe the system. The former allowed the quantification of the DO concentration heterogeneity observed in both the aerated and non-aerated section, leaving no doubts on the existence of a DO profile, proving that the well-mixed conditions assumption is incorrect (Rehman et al., 2017). The latter permitted the direct comparison between the TIS and the CFD-integrated modelling approaches. The DO concentrations predicted by both models showed a significant disparity, the difference being attributed to the well-mixed conditions assumption. Due to this hypothesis, the DO concentrations heterogeneities are hugely averaged out in the TIS model, thus making the values a bad representation of the average tank behaviour. Conversely, the CFD-integrated model can correctly describe the DO concentration profile along the reactor, since it takes into consideration mixing limitations. Therefore, the CFD-integrated model is a more suitable approach than the TIS model (Rehman et al., 2017).

Rehman and associates demonstrated with this work that the well-mixed condition is not verified in practice, which makes the present TIS modelling strategy inappropriate to describe the system oxygenation capacity (Rehman et al., 2017). To increase the understanding of the mechanisms involved in

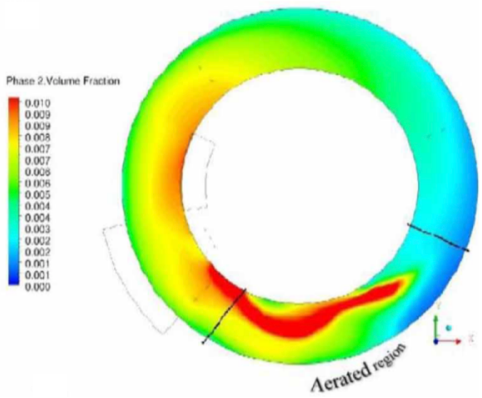

(a) Gas hold-up contour plots plots along the bioreactor

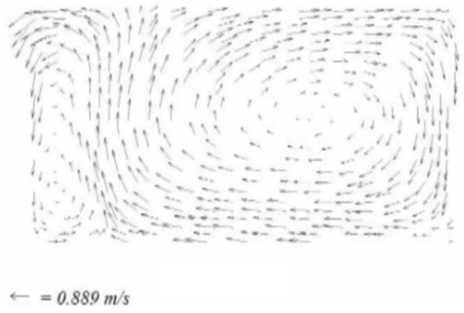

(b) Velocity vector plots at a vertical cross-section in the aerated region of the bioreactor.

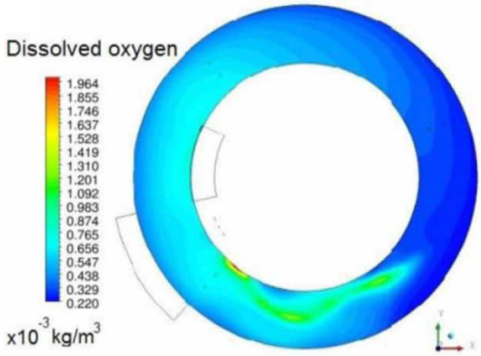

(c) DO concentration profile along the bioreactor.

Figure 2.6: Results of the CFD-integrated modelling approach developed by Rehman et al. (2017). Adapted from Rehman et al. (2017).

aeration, they proposed a novel approach based on CFD modelling, capable of accurately describing the DO profile along the reactor. Although the TIS modelling approach was proven to be inaccurate, the authors sustain that the CFD-integrated model should be used to improve it by helping the calibration process.

Although the model developed by Rehman and associates is an advancement in aeration modelling, it still has some limitations. These are mainly related to the consideration of a constant bubble size in the description of oxygen mass transfer. The work presented in section 2.5.2 aimed at improving this knowledge so that models like the one developed by this author could be optimised.

2.5.2 Impact of bubble size distribution dynamics

The state-of-the-art modelling of aeration efficiency strategies does not consider the impact of a varying bubble size on oxygen transfer. However, reports have been stating that bubble size distribution (BSD) is one of the key factors for its estimation (Shah et al., 1982; Sommer et al., 2017; Terashima et al., 2016; Wang and Wang, 2007). Although this discovery is not recent, there is still a knowledge gap regarding the impact of BSD dynamics on oxygen transfer (Amaral et al., 2017). In order to address this problem, Amaral and co-workers conducted a study in an aerated bubble column which aimed to create a new modelling strategy that explicitly involves the effect of BSD dynamics on oxygen transfer (Amaral et al., 2018). During this study, the researchers varied both the viscosity of the liquid phase and the air flow rates, because these parameters significantly influence BSD dynamics and, as such, the model must incorporate them. The development of this model led the researchers to address the shortcomings in the body of knowledge of the oxygen transfer field. Therefore, this work is not only an important benchmark to comprehend the effects of BSD dynamics on oxygen transfer, but also a crucial starting point for more accurate and complete oxygen transfer modelling approaches.

The research done by Amaral *et al.* comprised two different parts: experimental data collection (described in section 3.2) and modelling. The former was essential to determine important parameters that were used in the latter, such as local BSD dynamics and global gas holdups. Additionally, the global K_La was measured to experimentally validate the modelling method developed. The latter consisted in studying the effect of hydrostatic pressure on the local BSD dynamics and the modelling of both the local and global K_La. These concepts were first introduced in this work to highlight the dynamic character of oxygen transfer (Amaral et al., 2018). The local K_La refers to the volumetric mass transfer coefficient, measured in a section of the bubble column, and the global K_La to the volumetric mass transfer coefficient of the entire column. It is worth noting that until now only the concept of global K_La was used, as the BSD dynamics were always discarded.

Since the aim of this work was to study BSD dynamics, the calculation of the local K_La was crucial. To accomplish this task, the researchers divided the bubble column into sections and derived the BSD. For the former, seven sections were considered along the height of the column. The modelling of the local K_La was done for each section, thus seven values were determined. For the latter, Amaral and co-workers performed experiments (described in section 3.2) that allowed them to determine the bubble size. From these experiments, they were able to group the bubbles according to their size into classes, also named bins. The distribution of the bubbles by the bins led to the derivation of the BSD.

For the determination of the local K_La, the authors proposed a six-step modelling approach (Amaral et al., 2018). Firstly, the gas holdup in each bin, $\mathbf{V_{G,i}}$, was calculated by multiplying the local gas holdup (determined by assuming that the global gas holdup is uniformly distributed throughout the column) by

the ratio of the number of bubbles of the bin and the total number of bubbles in the section. This step was concluded with the determination of the gas holdup fraction in each bin, $\varepsilon_{G,i}$, using equation (2.20).

$$\varepsilon_{G,i} = \frac{\mathbf{V}_{G,i}}{\mathbf{V}_{G,i} + \mathbf{V}_L} \tag{2.20}$$

Secondly, the bubble terminal rising velocity in each bin, $\mathbf{u}_{b,i}$, was calculated using the correlation developed by Jamialahmadi and Muller-Steinhagen (1993). The parameter K_L was determined in each bin, $\mathbf{K}_{L,i}$, using equation (2.21) proposed by Higbie.

$$\mathbf{K}_{L,i} = \sqrt[2]{\frac{\mathbf{D}_L \times \mathbf{u}_{b,i}}{\pi \times \mathbf{d}_{b,i}}} \tag{2.21}$$

Here, $\mathbf{D}_L$ is the oxygen diffusion coefficient in the liquid and $\mathbf{d}_{b,i}$ is the bubble diameter equal to the mean of bin $\mathbf{i}$.

The interfacial area for mass transfer per unit volume in each bin, $\mathbf{a}_i$, was calculated by equation (2.22).

$$\mathbf{a}_i = \frac{6 \times \varepsilon_{G,i}}{\mathbf{d}_{b,i}} \tag{2.22}$$

The local K_La for each bin, K_La_i, was calculated by multiplying the results of equations (2.21) and (2.22). Lastly, the local K_La for the section was obtained by equation (2.23).

$$\mathbf{K}_L\mathbf{a}_{local} = \sum_i \mathbf{K}_{L,i} \times \mathbf{a}_i \tag{2.23}$$

Overall, seven local K_La were calculated. The modelled global K_La (respective to the entire column) was then obtained by adding the values of modelled local K_La for the different sections, multiplied by the volume ratio of each section.

The local BSD dynamics measurements allowed the authors to draw important conclusions. For tap water, it was observed that bubbles grow from the bottom to the top of the column due to the coalescence phenomenon (see section 2.5.2.A). Additionally, it was shown that hydrostatic pressure does not have a significant effect on bubble growth and that their growth is more pronounced at higher air flow rates. The measurements made with xanthan gum (XG) solutions (the author studied two XG solutions: one at concentration 0.2 (XG0.2) and other at 0.8 kg/m^3 (XG0.8)) corroborate the conclusions drawn for tap water. Yet, they also provided other important insights. It was possible to deduce that coalescence increases with increasing air flow rate, and more viscous solutions lead to bigger bubbles at the point of release and a decrease of the coalescence phenomenon. The global gas holdup analysis allowed to establish that this parameter increases with either increasing air flow rates or increasing liquid

viscosities. Finally, the results also exposed relationships between the global K_La and liquid viscosity or air flow rate. For the first, a non-linear variation was detected and for the second, the behaviour was akin to that previously described for the gas holdup.

The experimental and modelled global K_La are in good agreement for tap water and slightly differ for XG solutions. The authors justified this difference by questioning two assumptions made during the development of the modelling method. The first assumption was that the viscosity of XG solutions remained constant, even when the air flow rate increased. This is not true since these solutions behave as non-Newtonian fluids (Amaral et al., 2018). The second assumption was that the liquid phase was considered well-mixed, which is something that cannot be guaranteed (see section 2.5.1). Despite the influence of these assumptions, the modelled global K_La for the XG solutions were relatively close to the experimental values.

Finally, a representation of the local K_La along the height of the bubble column was made (Figure 2.7). A large variation of the local K_La throughout the column was reported for tap water; the difference being bigger when working with higher values of air flow rate. For XG solutions, this variation was smaller due to the increasing liquid viscosity. However, a significant variation was still registered for XG0.2.

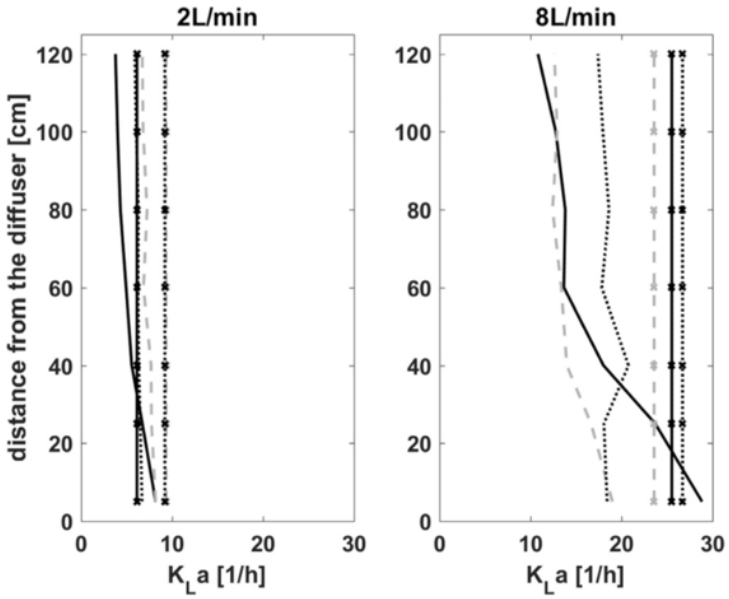

Figure 2.7: Variation of the local K_La along the height of the column. The black line represents tap water, the grey dashed line the XG0.2 solution and the black dotted line the XG0.8 solution. The lines without markers considered the local BSD dynamics whilst the lines with markers a constant bubble size. Adapted from Amaral et al. (2018).

From all the results presented, it was possible to draw several conclusions. Coalescence appears to be the main reason for bubble growth along the bubble column, increasing with air flow rate because the number of bubbles introduced into the system is higher. Hence, the probability of collision between

two bubbles is also higher. Conversely, coalescence reduces with higher liquid viscosity since this physical property hampers the movement of the bubbles, decreasing the probability of collision. The liquid viscosity seems to promote the formation of bigger bubbles because the bubbles take longer to be released, thus capturing more air. This work proves that oxygen transfer is influenced by both gas holdup and bubble size. Due to the influence of these two parameters, there is no linear relation between the K_La and increasing liquid viscosity, since both K_L and a are differently influenced (see equations (2.22) and (2.23)). This leads to the conclusion that oxygen transfer results from a trade-off between these parameters, which vary along the height of the column, as proven by the variation of the local K_La (Figure 2.7). Therefore, this work clearly demonstrates the dynamic character of oxygen transfer due to its strong dependence on BSD dynamics, which are in turn affected by both wastewater characteristics (such as viscosity) and hydrodynamic parameters (such as air flow rate). Bearing all these conclusions in mind, the influence of BSD dynamics cannot be discarded in order to improve state-of-the-art aeration modelling approaches.

2.5.2.A The coalescence phenomenon

The evolution of bubble size in multiphase flows, namely in gas-liquid reactors, is determined by numerous processes, such as mass transfer, breakup, and coalescence (Liao and Lucas, 2010). The first is related to the movement of molecules, contrary to the concentration gradient, between phases (see section 2.3.1.A). The second is associated with the breakup of bubbles, i.e. one gas bubble breaks up creating two or more smaller bubbles. Finally, coalescence refers to the creation of a new bubble resulting from the collision of two or more distinct bubbles. Since coalescence was identified as the primary reason for the evolution of the bubble size in the bubble column under study, this process is highlighted.

Coalescence is part of a larger group of processes called aggregation processes. In the specific case of coalescence, the newborn particle results from the complete merging of the colliding particles (case of the air bubbles). Another type of aggregation mechanism is coagulation, where flocs of particles are loosely held together by surface forces, thus not involving physical contact (Nopens, 2005). As previously mentioned, out of all aggregation processes, the most meaningful for the studied system is coalescence because it dictates BSD. Therefore, the remaining part of this section explores the theories developed to explain coalescence, as well as the different mechanisms involved in this complex process.

Three different theories have been proposed to explain coalescence, the most popular one being the film drainage model. This theory was developed by Shinnar and Church and describes coalescence as a three-stage process. The first step involves the collision of two bubbles that are not immediately capable of merging due to the presence of a small amount of liquid trapped between them. Next, the attractive forces drive the liquid film to drain out to a critical thickness. Finally, the film ruptures and the bubbles

coalesce. This theory also recognises that not all collisions will result in coalescence and, as such, the concept of coalescence efficiency needs to be introduced. It should be noted that the calculation of this parameter is directly related with the theory used to describe coalescence (Liao and Lucas, 2010). In this case, the determination of the coalescence efficiency is done with respect to the film drainage theory.

Despite the existence of different coalescence theories, they all agree that contact and collision are the premise of the process. Therefore, one major concern when facing the coalescence process is the adequate description of mechanisms that can produce collisions. In a turbulent flow, there are at least five sources of relative motion: (1) motion induced by turbulent fluctuations in the surrounding continuous phase, (2) motion induced by mean-velocity gradients, (3) different bubble rise velocities induced by buoyancy or body forces, (4) bubble capture in an eddy , (5) wake interactions or helical/zigzag trajectories (Liao and Lucas, 2010). Even though one can identify these five sources, they are not present in every situation, as their prevalence varies with operating conditions, such as air flow rate and liquid viscosity. Furthermore, depending on the case, some of them can greatly influence coalescence and others may be insignificant. Bearing this in mind, it is crucial to identify which ones are relevant in each specific application to correctly predict the collision frequency.

In the last two paragraphs, the most noteworthy theory behind coalescence was described and detailed. Additionally, the concepts of coalescence efficiency and collision frequency were introduced. In section 3.3.1.A, the mathematical approach and a model to determine coalescence frequency are presented.

2.6 Summary

In this chapter, the reader was introduced to the wastewater engineering scientific field and one of its major challenges: aeration. The importance, types, and bottlenecks of aeration in wastewater treatment were discussed. At this point, mathematical modelling of oxygen transfer was identified as a possible way to overcome the current obstacles. To better understand the physical phenomena behind oxygen transfer, the gas-liquid mass transfer theory was detailed and the volumetric oxygen transfer coefficient - K_La - presented. The measurement of this key parameter to oxygen transfer, as well as the state-of-the-art modelling strategies were described and the major knowledge gaps pinpointed. One of them is the assumption of perfectly mixed conditions, addressed in the CFD integrated model developed by Rehman et al. (2017). The second is related to the poor understanding of the influence of BSD on oxygen transfer. This was explored by reviewing the model developed by Amaral et al. (2018).

Considering the literature review presented, it is clear that there is a knowledge gap associated with BSD. Therefore, the focus of this research was directed towards the comprehension of BSD in view of the need of understanding its impact on oxygen transfer.

3

Model Development

Contents

As stated in section 1.2, the goal of this thesis is to continue the work of Amaral et al. (2018) by developing a model that predicts the BSD dynamics observed in the bubble column. Due to the complexity of developing such a model, an overview of the concepts, their relationships, and the steps involved in the modelling exercise is provided. Moreover, the sections in which each of these steps are presented are indicated in Figure 3.1 to guide the reader through this chapter.

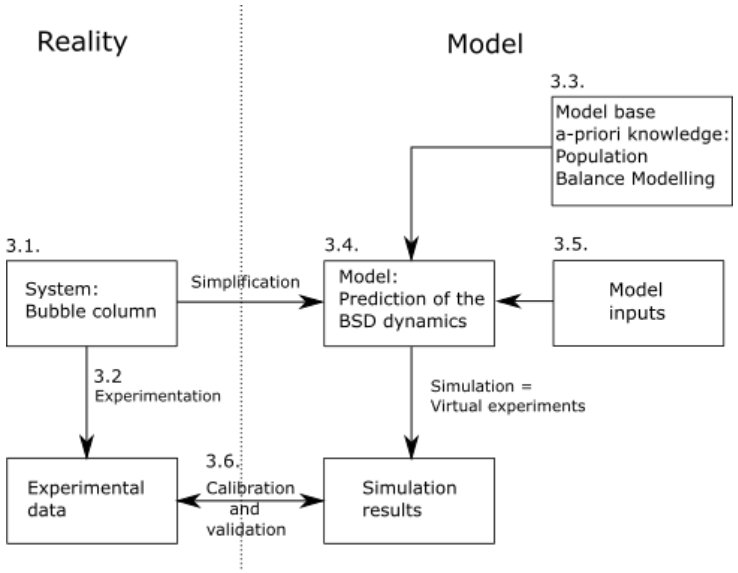

Figure 3.1: Overview of the modelling exercise. The numbers are associated with the steps and indicate the sections of chapter 3 in which they are explained. Adapted from Makinia (2010).

According to Makinia (2010), a model is a description of a system. The system is a set of various interrelated elements within boundaries, that interact with one another in an organised fashion toward a common, specific objective. In this case, the system is the bubble column and the model describes the BSD dynamics observed. Since the system is too complex to be fully described, there is a need to simplify it. In fact, the golden rules of the modelling exercise state that "no model is perfect, some are useful" and "a model should be as simple as possible, and only as complex as needed" (Makinia, 2010). The simplification of reality is often achieved through considerations about the system at hand. The assumptions that result from these considerations limit the applicability of the model, because they are not always verified. Therefore, it is of the utmost importance to know how the modeller described the system and for which cases that description is valid. The description of the system as well as the assumptions considered can be found in section 3.1.

In section 3.2, the process of generating system behaviour and gathering data – experimentation (Makinia, 2010) – is presented. This step is what produces the information that allows the modeller to know how the system behaves. There are two big concerns associated with experimentation. On the one hand, the experimental equipment used to measure the behaviour of the system often has limitations. This leads to more assumptions that influence the model and, as such, needs to be discussed. On the

other hand, since the model aims to mimic the data obtained by experimentation, the ability to compare model results with experimental results is crucial. As errors in the experimental data strongly affect the quality of the model developed, the experimentation process that originated the data used in this thesis is thoroughly described. The importance of experimental data reliability is explored in section 3.6.

Even though many assumptions are considered to simplify the system, its description often remains complex, thus the comprehension of the mathematical background needed to describe it is essential. In section 3.3, the mathematical framework used to predict BSD dynamics - Population Balance Modelling (PBM) – is presented. Due to the inherent complexity of this strategy, its numerous concepts are introduced and the main equations shown. After, the mathematical description of the coalescence phenomenon (its relevance was already discussed in sections 2.5.2 and 2.5.2.A) and its relationship to the PBM framework are studied. The section ends with the description of the method – Fixed Pivot Technique (FPT) - used to solve the complex equations obtained.

In section 3.4, the knowledge acquired from sections 3.1 to 3.3 is applied to formulate the model. As the model used to describe the coalescence frequency had to be modified, the modifications are presented. Moreover, the insertion of this term into the Population Balance Modelling Equation (PBME) is highlighted.

Section 3.5 focuses on the model inputs, required from both the FPT (grid definition) and PBM framework (initial condition).

Finally, section 3.6 aims to detail both the calibration and validation processes. The former is fundamental to obtain a useful model, while the latter allows the modeller to check if the simulation results match the experimental observations. Here, the reliability of the experimental data plays a crucial role, because it is used to refine the model obtained in section 3.4.

3.1 Description of the system

The system under study is a lab-scale cylindrical bubble column reactor aerated with a diffuser. The air enters at the bottom of the reactor in the form of bubbles. As soon as the bubbles enter the system, a distribution of sizes is formed, i.e. a BSD. The bubbles rise through the vessel due to their buoyancy and, during the climb, they are subjected to phenomena that can induce bubble coalescence. The bubbles leave the system at the top of the reactor by breaking the liquid surface.

To describe the BSD in this system, the following assumptions were considered:

- The bubbles are assumed to be rigid spheres to facilitate its geometrical description.
- The growth of the bubbles due to differences in hydrostatic pressure is discarded, because the weight of the liquid column is not significant. In addition, differences caused by gas-liquid mass

transfer are neglected, since it is assumed that the liquid is saturated in oxygen. Therefore, the only phenomenon influencing bubble size is coalescence.

- Bubbles rise at the terminal rising velocity, which is dependent on their size. According to Amaral et al. (2018), this velocity is the maximum velocity achieved by the bubble when the net force acting on the bubble is equal to zero. The influence of bubble swarms on this velocity is disregarded. Furthermore, it is considered that the bubbles detach from the diffuser with this velocity.
- Analogously to the strategy described by Amaral et al. (2018) (see section 2.5.2), bubbles that have similar sizes can be grouped in the same class, also referred to as bin. Once the bubbles are grouped in the same bin, the bubbles share the same characteristics, namely size. The group of all size bins covers the entire population of bubbles observed. When the number of bubbles in each bin is identified, the BSD can be derived.

3.2 Experimental data collection

The experimentation process described was not performed by the author. However, due to its importance for the work developed, it is described. For further reading, the reader is referred to Amaral et al. (2018).

The experiments were conducted in a bubble column reactor aerated with a diffuser (Figure 3.2(a)). The air flow rates used were 2, 4, 6, and 8 L/min and could always be described as homogeneous bubbly flow because the air velocity never surpassed 0.05 m/s (Shah et al., 1982). Three different solutions were used as liquid phase: tap water and xanthan gum (XG) solutions at concentrations of 0.2 and 0.8 kg/m^3. The XG solutions mimicked the viscosity of AS, which is an important parameter to account for in oxygen transfer. The measurement of BSD dynamics was performed using a high-speed camera (Figure 3.2(a)) that made three videos of at least 1000 images with a spatial resolution of 0.095 ($\pm$0.005) mm/pixel at seven different heights of the column (Figure 3.2(b)). The section photographed was the one at the centre of the column. The images were treated with the digital image analysis proposed by Bellandi et al. (2016), which allowed the determination of bubble size (Figure 3.2(a)). The bubbles were then divided into bins and the number of bubbles in each bin was calculated. This information enabled the construction of the cumulative BSD. It should be noted that, during measurements, the bulk liquid was saturated with DO, thus preventing gas-liquid mass transfer. The global gas holdup was determined by measuring the difference between the liquid level at steady state during gas injection and the liquid level without gas injection. The gas holdup for each section was then calculated by assuming an uniform distribution along the height of the column.

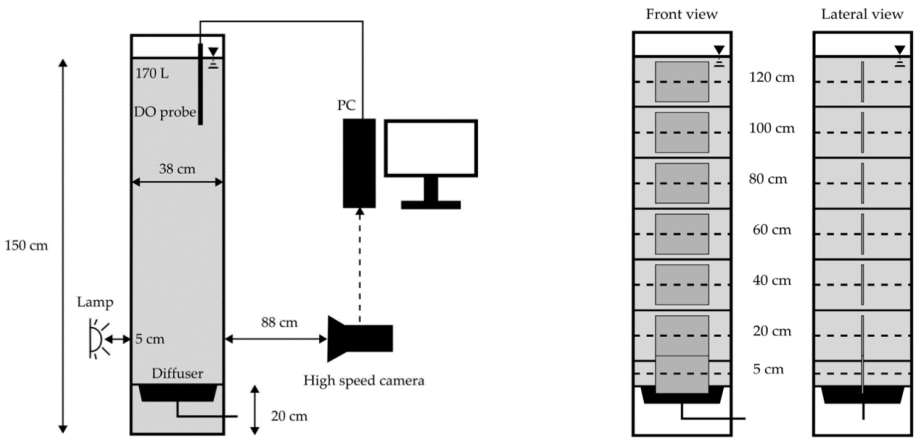

(a) Experimental set-up.

(b) Sections defined along the height of the column.

Figure 3.2: Experimental set-up and definition of column sections. Adapted from Amaral et al. (2018).

Now that the experimentation process has been described, its main limitations must be addressed. The first is related to the fact that both the water and XG solutions are not pure, thus the presence of species that influence interface characteristics cannot be neglected. The second is associated with the fact that only the centre of the column was photographed. Therefore, there was a need to assume that the BSD at the centre was an adequate representation of the BSD of the section. The third is linked to the digital image analysis strategy developed by Bellandi et al. (2016) used to identify the bubbles, because it introduces possible errors in bubble identification. These arise from the fact that bubbles were considered as spheres, yet not all bubbles are spherical. Finally, the measurement of the local gas holdup has an error associated, since it is based on the assumption that the gas is uniformly distributed throughout the reactor.

This experimental methodology considered seven sections, four airflow rates, and three different solutions. Therefore, eighty four BSD were measured. The following nomenclature was used: (1) CW, XG0.2, and XG0.8 stand for clean water, xanthan gum at 0.2 kg/m^3, and xanthan gum at 0.8 kg/m^3, respectively; (2) 2, 4, 6, and 8 denote the airflow rate (in L/min); and (3) sections 5, 20, 40, 60, 80, 100, and 120 represent the distance from the diffuser (in cm) at which BSD was measured. This notation was also used to compare experimental and simulation results.

3.3 Mathematical background - Population Balance Modelling

In this section, the framework of PBM is defined and its relevance for the present work highlighted. The PBME is formulated and a brief introduction regarding the existence of solution initiated. The notation and terminology necessary to comprehend the PBME formulation is provided in Annex A. Next, the coalescence phenomenon is mathematically described and its association with the PBM framework explained. The section ends with the description of the method used to solve the resulting PBME, the FPT.

3.3.1 Definition and relevance of the framework of PBM

The PBM framework is used when one is concerned with systems consisting of particles dispersed in an environmental phase, which is referred to as the continuous phase. The particles can be solid granules, gas bubbles or liquid droplets which may interact between themselves as well as with the continuous phase. Each particle is associated with a number of properties (see section A.1), that vary with time and affect the aforementioned interactions (Ramkrishna, 2000). Hence, the behaviour of a particle in the system is dependent on its group of properties.

The evolution and overall behaviour of the system described is dictated by the evolution of the particles (Yeoh et al., 2014). Therefore, the understanding and description of all the phenomena that can influence the particle state throughout time is crucial. According to Ramkrishna (2000), the rate of change of state of any particle is a function of the state of the particle and the local continuous phase variables. Thus, the particle state can only change due to evolutionary processes such as nucleation, growth, dispersion, dissolution, aggregation or coalescence, and breakage or due to the transport of the particle phase in the system (Yeoh et al., 2014). To account for the latter event in the PBM approach, the coupling of transport equations to the PBM is necessary (Ramkrishna, 2000). Although the PBM approach considers both the particle state and the continuous phase, its main concern is the tracking of the number of entities within the system (Yeoh et al., 2014). Hence, the PBM framework is a mathematical procedure that tracks the number of entities – solid particles, bubbles or droplets – present within a system, considering their development and interactions with themselves as well as with the continuous phase.

Even though the PBM framework was developed long ago, its rise to influence in the scientific community only started after the publication of the general version in the late seventies. After that, there has been a steep increase in the application of PBM throughout various scientific fields (Ramkrishna and Singh, 2014). Despite this increase in popularity, there are still research fields that have yet to benefit from this framework; wastewater treatment being one of them (Nopens et al., 2015). Nopens and associates (Nopens et al., 2015) developed work to raise the awareness about the PBM framework

in the wastewater treatment community, thus hoping to encourage the application of this powerful modelling tool in the field. According to the authors, many of the processes involved in wastewater treatment deal with distribution of properties under transient conditions, such as bubble size, floc size, crystal size or granule size. Since PBM can describe the dynamics of properties that are characterised by distributions, the application of this modelling approach can develop new knowledge and increase the predictive capability of the current models.

As previously stated (see section 1.2), the objective of this thesis is to continue the work of Amaral et al. (2018) which deals with a population of bubbles and needs to describe its BSD dynamics. As shown by Nopens et al. (2015), PBM is an ideal framework to describe and understand this property. Therefore, the understanding and application of this methodology is essential to the success of this work.

3.3.2 The Population Balance Modelling Equation

The general PBME is denoted by equation (3.1). To better understand its formulation, the reader is referred to Annex A, where all the basic concepts are thoroughly presented and detailed.

$$\frac{\partial}{\partial t} f_1 + \nabla_x \cdot (\mathbf{v_x} f_1) + \nabla_r \cdot (\mathbf{v_r} f_1) = h \tag{3.1}$$

The first term on the left-hand side of equation (3.1) characterises the local change of the particle number density with time (i.e. the accumulation term). The second term represents the change of the number density due to advection in the external coordinates, while the third term denotes the change of the number density due to advection in internal coordinates, indicating several particle growth phenomena. These two terms correspond to continuous processes. The term on the right-hand side of equation (3.1) is the net rate of generation of particles and represents the discrete processes (see section A.6) (Nopens, 2005; Ramkrishna, 2000; Yeoh et al., 2014).

Finally, the PBME must be supplemented with initial and boundary conditions (Ramkrishna, 2000). The initial condition must clearly stipulate the distribution of particles in the particle state space, including internal and external coordinates at time zero, while the boundary conditions must describe what happens in the boundaries of the system. The latter is strongly dependent on the characteristics of the system (Ramkrishna, 2000).

3.3.2.A Existence of solution

The attempts to solve an equation can only be successful if there is a solution to be found. Thus, one of the biggest concerns when dealing with mathematical equations is the existence of such solution.

For the case of the PBME, the existence of solution is dependent on the characteristics of the right-hand side, i.e. the net rate of generation of particles function (Nopens, 2005). According to Ramkrishna (2000), there are three possible scenarios for this function. For two of the three cases, the obtained equation is a first-order partial differential equation (the existence of solution is well known) while for the other case the PBME becomes an integro-partial differential equation which is more complex. However, the existence of solution is assured by the convergence of the method of successive approximations (Ramkrishna, 2000). Therefore, the PBME can be solved in all three cases. For further reading, the reader is referred to (Ramkrishna, 2000).

3.3.3 Coalescence in the PBME

Up until this point, the concern has only been with how the particle population redistributes itself in the particle state space throughout time, since the death and birth of particles were grouped in a single term – the net rate of generation of particles. However, the detailed study of the birth and death processes is the crux of PBM because it allows us to understand how particles appear and disappear in the system, rather than merely knowing how they are redistributed. The entities present within the system can appear or disappear within the boundaries of the internal particle state space or at any point in the particle state space (Ramkrishna, 2000). The latter, which is directly related with the aggregation/coalescence, breakage, and nucleation processes, will be the target of this section.

Out of the processes mentioned, coalescence is the only one observed in the experiments which are the basis for this thesis and, thus, the one further explained. The coalescence process described herein is solely valid for binary coalescence (collision between two particles) and is insensitive to the degree of physical contact, which means that it accounts for coagulation events too. Due to these limitations, the mathematical derivation presented is most suitable to describe diluted systems because the reduced number of entities ensure that the binary event is the most probable one (Nopens, 2005).

Firstly, one should define the net generation rate due to coalescence processes, $h_C(\mathbf{x},\mathbf{r},\mathbf{Y},t)$, which can be decomposed into a source term, $h_C^+(\mathbf{x},\mathbf{r},\mathbf{Y},t)$, and sink term, $h_C^-(\mathbf{x},\mathbf{r},\mathbf{Y},t)$. The former represents the birth of particles of size $\mathbf{x}$ due to coalescence processes and the latter the death of particles of size $\mathbf{x}$ due to coalescence processes. A schematic representation of the source and sink terms can be seen in Figure 3.3.

Secondly, a coalescence frequency is defined, $\Gamma(\tilde{\mathbf{x}},\tilde{\mathbf{r}};\mathbf{x}',\mathbf{r}',\mathbf{Y},t)$, which represents the fraction of pairs of particles of states ($\mathbf{x}$,$\mathbf{r}$) and ($\mathbf{x}$',$\mathbf{r}$') that coalesce per unit of time. The frequency is independent of the ordering of the pairs of particles and, as such, symmetric ($\Gamma(\mathbf{x}',\mathbf{r}';\tilde{\mathbf{x}},\tilde{\mathbf{r}},\mathbf{Y},t) = \Gamma(\tilde{\mathbf{x}},\tilde{\mathbf{r}};\mathbf{x}',\mathbf{r}',\mathbf{Y},t)$). Furthermore, the state of the particle as a result of coalescence needs to be identified and defined. To do so, it is assumed that by knowing both the state of the new particle ($\mathbf{x}$,$\mathbf{r}$) and the state of one of the coalesc-

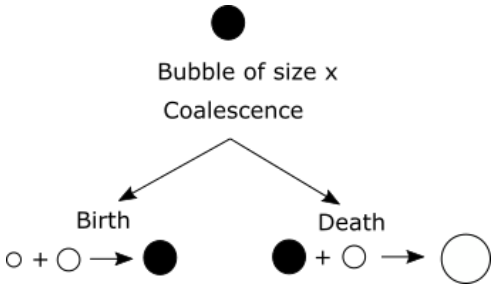

Figure 3.3: Birth and death of a generic bubble due to the coalescence process. Adapted from Nopens (2005).

ing particles (**x**',**r**'), the state of the other coalescing particle can be determined and it is denoted by $[\tilde{\mathbf{x}}(\mathbf{x},\mathbf{r}|\mathbf{x}',\mathbf{r}'),\tilde{\mathbf{r}}(\mathbf{x},\mathbf{r}|\mathbf{x}',\mathbf{r}')]$ (Ramkrishna, 2000).

Thirdly, it is necessary to define the average number of pairs of particles at each instant t with specified states. Therefore, the average number of distinct pairs of particles at time t per unit volume in state space located about (**x**,**r**) and (**x**',**r**') is designated by f_2(**x**,**r**;**x**',**r**',t) (Ramkrishna, 2000). Finally, one can write the net generation rate due to coalescence processes, h_C(**x**,**r**,**Y**,t), as the difference between the source and sink terms:

$$\begin{aligned} h_C(\mathbf{x},\mathbf{r},\mathbf{Y},t) &= h_C^+(\mathbf{x},\mathbf{r},\mathbf{Y},t) - h_C^-(\mathbf{x},\mathbf{r},\mathbf{Y},t) \\ &= \int_{V_\mathbf{x}} \frac{1}{\delta}\,\Gamma(\tilde{\mathbf{x}},\tilde{\mathbf{r}};\mathbf{x}',\mathbf{r}',\mathbf{Y},t)\,f_2(\tilde{\mathbf{x}},\tilde{\mathbf{r}};\mathbf{x}',\mathbf{r}',t)\,\frac{\partial(\tilde{\mathbf{x}},\tilde{\mathbf{r}})}{\partial(\mathbf{x},\mathbf{r})}\,dV_\mathbf{x} \\ &\quad - \int_{V_\mathbf{x}} \Gamma(\mathbf{x},\mathbf{r};\mathbf{x}',\mathbf{r}',\mathbf{Y},t)\,f_2(\mathbf{x},\mathbf{r};\mathbf{x}',\mathbf{r}',t)\,dV_\mathbf{x} \end{aligned} \tag{3.2}$$

In equation (3.2), δ represents the number of times identical pairs have been considered ($1/\delta$ corrects the redundancy) and the term $\frac{\partial(\tilde{\mathbf{x}},\tilde{\mathbf{r}})}{\partial(\mathbf{x},\mathbf{r})}$ represents the Jacobian determinant, which is used to transform the density in coordinates to one in terms of (**x**,**r**). It should also be noticed that both equations are only written with respect to the internal coordinates, because the birth or death of a particle takes place at the same location where the parent particles coalesce (Yeoh et al., 2014). The last consideration is associated with an approximation necessary to close equation (3.1) when the right-hand side is replaced by equation (3.2). The approximation, illustrated by equation (3.3), represents the coarsest form of closure hypothesis and implies that there is no statistical correlation between particles of states (**x**',**r**') and (**x**,**r**) at any instant t (Ramkrishna, 2000).

$$f_2(\tilde{\mathbf{x}},\tilde{\mathbf{r}};\mathbf{x}',\mathbf{r}',t) \approx \tilde{f}_1(\tilde{\mathbf{x}},\tilde{\mathbf{r}},t) f_1{}'(\mathbf{x}',\mathbf{r}',t) \tag{3.3}$$

3.3.3.A Coalescence kernels - The model of Prince and Blanch

To solve equation (3.2), closure is required for the coalescence frequency term, Γ(**x**,**r**;**x**',**r**',**Y**,*t*). Numerous physical models have been developed to mathematically describe this term. These models are usually called coalescence kernels. Among them, the kernel developed by Prince and Blanch (1990) was used in this thesis to determine the coalescence frequency. The model was selected due to its nature (it was developed for air-sparged bubble columns) and simplicity (reflected by the existence of only one coefficient/correction factor). It should be noted that factors involved in this kind of model are difficult to accurately measure, thus an elevated number of coefficients usually leads to more uncertain models. As mentioned in section 2.5.2.A, there are two concepts involved in coalescence frequency which are the collision frequency and coalescence efficiency. These terms are related by equation (3.4).

$$\Gamma_{j,k} = \theta_{j,k} \times \lambda_{j,k} \tag{3.4}$$

As discussed in section 2.5.2.A, the determination of the collision frequency, $\theta_{j,k}$, relies on the mechanisms considered to promote collisions, whereas the calculation of the coalescence efficiency, $\lambda_{j,k}$, relies on the theory used to explain coalescence. The model developed by Prince and Blanch (1990) accounts for three sources of collision, assumed to be additive, and uses the film drainage theory to describe coalescence.

The authors considered that collisions could occur due to three different mechanisms: (1) turbulence, (2) buoyancy, and (3) laminar shear. Turbulence can cause collisions since it is responsible for the random motion of bubbles. Buoyancy driven collisions are related to the presence of various bubble sizes. Due to the different sizes, bubbles have different rise velocities, which can lead to collisions. The final mechanism - laminar shear - represents collisions that may arise from the variety of hydrodynamic regimes present in the bubble column. Some of them create regions of high liquid velocity, which may cause the bubbles located there to collide with bubbles present in a slower velocity field. Bearing this in mind, one can now consider the mathematical derivations of each mechanism.

To guarantee that the turbulence problem is tractable, two assumptions were made by the authors: (1) turbulence is isotropic (i.e. uniform in all directions) and (2) the bubble size lies in the inertial subrange (the bubble size is comparable to an intermediate range of turbulent scales). Additionally, the random motion of fluid particles in a turbulent flow is assumed to be analogous to the random movement of gas molecules in an ideal gas (Prince and Blanch, 1990). Considering these assumptions, equation (3.5) is deduced.

$$\theta_{j,k}^{T} = C_1^{'} \left(d_j + d_k\right)^2 \left(d_j^{2/3} + d_k^{2/3}\right)^{1/2} \varepsilon^{1/3} \tag{3.5}$$

In equation (3.5), $\theta_{j,k}^{T}$ represents the turbulent collision rate of bubbles j and k, $C_1^{'}$ is, according to Liao and Lucas (2010), an adjustable parameter that can vary between 0.28 and 1.11, d_j and d_k are the diameters of the bubbles involved in the collision, and ε is the turbulent energy dissipation rate, which can be determined by equation (3.6).

$$\varepsilon = \frac{Qg}{\pi R_T^2} \frac{P_2\, ln(P_1/P_2)}{P_1 - P_2} \tag{3.6}$$

In equation (3.6), Q is the volumetric gas flow rate, g is the acceleration of gravity, R_T is radius of the bubble column, and P_1, P_2 are the pressures at the bottom and top of the column, respectively.

The collisions resulting from buoyancy are calculated with the expression presented in equation (3.7).

$$\theta_{j,k}^{B} = S_{j,k}\, |u_{r,j} - u_{r,k}| \tag{3.7}$$

In equation (3.7), $\theta_{j,k}^{B}$ denotes the buoyancy-driven collision rate of bubbles j and k, $S_{j,k}$ is the collision cross-sectional area (equation (3.8)) which depends on the diameters of bubbles j and k, and $u_{r,j}$ and $u_{r,k}$ are the rising velocities of bubbles j and k (equations (3.9) to (3.11)).

$$S_{j,k} = \frac{\pi}{4} (d_j + d_k)^2 \tag{3.8}$$

$$u_r = \frac{u_s\, u_w}{\sqrt{u_b^2 + u_w^2}} \tag{3.9}$$

$$u_s = \frac{g\, (\rho_L - \rho G)\, d_b^2}{18\, \mu_L} \frac{3\, \mu_L + 3\, \mu_G}{2\, \mu L + 3\, \mu_G} \tag{3.10}$$

$$u_w = \sqrt{\frac{2\, \sigma_L}{\rho_L\, d_b} + 0.5\, g\, d_b} \tag{3.11}$$

In equations (3.10) and (3.11), g is the acceleration of gravity, ρ_L and ρ_G are the liquid and gas densities, μ_L and μ_G represent the liquid and gas viscosities, σ_L denotes the liquid surface tension, and d_b the bubble's diameter. It should be noted that equations (3.9) to (3.11) only hold for single-bubbles, thus they do not account for bubble swarms. Moreover, the effect of surfactants on the rising velocity is neglected.

Finally, collisions caused by laminar shear rate are accounted for by equation (3.12). The construction of this equation is based on two assumptions: (1) the system is inviscid and (2) the average shear rate can be found by averaging the local shear rate over the radial dimension of the column (Prince and Blanch, 1990).

$$\theta_{j,k}^{LS} = \frac{4}{3}(r_j + r_k)^3\, 5.3\, \frac{U_{l,max}}{R_T} \tag{3.12}$$

In equation (3.12), $\theta_{j,k}^{LS}$ is the collision rate due to laminar shear rate, r_j and r_k are the radius of bubbles j and k, $U_{l,max}$ is the maximum liquid circulation velocity , and R_T the radius of the bubble column. Since the mechanisms are assumed to be additive, the expression that calculates the total collision frequency, $\theta_{j,k}$, is illustrated by equation (3.13).

$$\theta_{j,k} = \theta_{j,k}^{T} + \theta_{j,k}^{B} + \theta_{j,k}^{LS} \tag{3.13}$$

Prince and Blanch (1990) used the film drainage theory to describe coalescence. Hence, the coalescence efficiency expression is a function of the drainage, rupture, and contact times. The first is associated with the time required for the film trapped between the two bubbles to drain. The second is related to the time needed for the liquid film to rupture. The sum of these two times is the coalescence time and represents the time required for the bubbles to merge. The third corresponds to the time they are close enough for coalescence to take place. The probability of a collision resulting in coalescence relies on the relationship between the coalescence and contact times. The coalescence efficiency expression (equation (3.14)) can be deduced in two steps. In the first, the coalescence and contact times are assumed to be random variables and the coalescence time to be normally distributed. In the second, the expression for the probability of coalescence based on the normal distribution is simplified by assuming that the standard deviation for the coalescence time is zero, i.e. the coalescence time is not distributed (Tsouris and Tavlarides, 1994).

$$\lambda_{j,k} = exp(-\frac{t_{j,k}}{\tau_{j,k}}) \tag{3.14}$$

In equation (3.14), λ represents the coalescence efficiency, $t_{j,k}$ the time required for coalescence of bubbles of radius r_j and r_k (equation 3.15), and $\tau_{j,k}$ the contact time between bubbles j and k (equation 3.17).

$$t_{j,k} = (\frac{r_{j,k}^3\, \rho_L}{16\, \sigma_L})^{1/2}\, ln\frac{h_0}{h_f} \tag{3.15}$$

Here h_0 is the initial film thickness, h_f the critical film thickness, and $r_{j,k}$ the equivalent radius that can be calculated with equation (3.16) if the radius of bubbles j and k are known. According to Liao and Lucas (2010), h_0 and h_f usually take the values of $10^{-4}\, m$ and $10^{-8}\, m$, respectively.

$$r_{j,k} = \frac{1}{2}(\frac{1}{r_j} + \frac{1}{r_k})^{-1} \tag{3.16}$$

It is important to note that equation (3.15) can only be derived if these assumptions are considered: (1) the rupture time is neglected, because the concentration of surfactant species is equal to zero; (2) the gas-liquid interface is mobile; (3) the Hamacker constant, which accounts for the mutual attraction of molecules on opposite sides of the liquid film, is disregarded; (4) the effect of bubble deformation by turbulent eddies is not considered; and (5) the radius of the liquid disk between coalescing bubbles is the bubble radius.

$$\tau_{j,k} = \frac{r_{j,k}^{2/3}}{\varepsilon^{1/3}} \tag{3.17}$$

Equation (3.17) is derived solely from dimensional considerations and can only be regarded as an order of magnitude approximation (Prince and Blanch, 1990). Furthermore, the choice of the characteristic length, $r_{j,k}$, is considered to be arbitrary.

Equations (3.5), (3.7), (3.12), (3.15), and (3.17) sum up the model developed by Prince and Blanch (1990). These equations were used as a basis for the coalescence kernel developed, which in turn led to the determination of BSD dynamics.

3.3.4 Solution methods

Due to the inherent complexity of PBMEs, analytical solutions to these equations can only be found in idealised situations or simplified cases. Therefore, the successful use of PBMEs relies on our ability to solve them numerically (Kumar and Ramkrishna, 1996a). To support this necessity, several numerical solution methods (SMs) have been proposed throughout the years. In this section, a simplified overview of the existent SMs and a brief discussion of their characteristics is presented. In addition, the numerical SM named Fixed Pivot Technique (FPT), used to develop the work presented in this thesis, is introduced and detailed.

3.3.4.A Overview of the existing SMs

As mentioned before, PBMEs are mostly solved by numerical methods because analytical solutions only exist for idealised or simplified cases (Kumar et al., 2006). The numerous SMs described in the literature to solve the PBME can be divided into five groups: finite element methods, finite volume methods, stochastic methods, moment methods, and sectional methods. The differences between each group are mainly related with computational burden, accuracy, efficiency, robustness, and stability (Giri and Hausenblas, 2013). Besides that, the phenomena that can be described by each group of SMs, such as growth, aggregation/coalescence, nucleation or breakage, can also differ.

According to Giri and Hausenblas (2013), the SMs that are most used are part of the sectional

methods group. The reason behind their popularity is linked to the ability to accurately predict selected moments of the distribution, while giving satisfactory results for the complete density distribution. Due to these characteristics, this type of method has become very attractive computationally. Therefore, several authors have focused on developing sectional methods; being the most famous ones: the FPT (Kumar and Ramkrishna, 1996a), the moving pivot technique (MPT) (Kumar and Ramkrishna, 1996b), and the cell average technique (CAT) (Kumar et al., 2006). Although the FPT is not the best sectional method, since it consistently over-predicts the resulting number density and its higher moments, this technique is currently the most used method due to its generality, robustness, and efficiency (Giri and Hausenblas, 2013; Kumar et al., 2006).

3.3.4.B The Fixed Pivot Technique

The FPT is a numerical SM, developed by Kumar and Ramkrishna (1996a), which relies on the discretisation of the PBME. All the sectional methods mentioned in section (3.3.4.A) divide the distribution domain into a given number of classes, also called bins or cells. The strategy allows the transformation of the continuous population balance equation into a set of ordinary differential equations (ODEs), because a balance equation is applied to each bin. The discretisation of the PBME facilitates the resolution process, since the resulting equations are simple to solve and have no explicit size dependency (Kumar et al., 2006). The set of ODEs is represented in equation (3.18).

$$\frac{dN_i}{dt} = B_i - D_i \tag{3.18}$$

In equation (3.18), N_i is the number concentration of particles within bin i while B_i and D_i are the birth and death rates in the ith bin, respectively. Equation (3.18) shows the general version of the discretised PBME. Nonetheless, this equation still needs to be detailed, especially the terms on the right-hand side. There are several ways to develop these terms, thus the numerous differences between the SMs. However, as previously mentioned, the method that will be characterized is the FPT developed by Kumar and Ramkrishna (1996a). It is worth noting that the discretisation process discards the influence of continuous processes. Therefore, equation (3.18) is only valid if one assumes that there is no particle growth or nucleation and the system is perfectly mixed.

Kumar and Ramkrishna (1996a) started by dividing the entire size range into small sections (the authors did not consider a specific domain but rather a general domain). The next step consisted in defining two types of points in this space: (1) points which limit a section, v_i and v_{i+1} and (2) points within a section that represent the section's particle population, x_i, such that $v_i < x_i < v_{i+1}$. The sections contained between the points v_i and v_{i+1} are named the ith cell and the points x_i are called pivot or grid points. The most remarkable characteristic of this grid is its flexibility since the grid can

either be uniform or geometric. Furthermore, the grid can be fine in some size ranges and coarse in others. A visual representation of a generic uniform grid is shown in Figure 3.4.

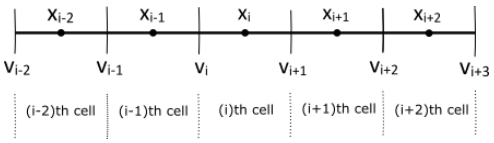

Figure 3.4: A generic uniform grid used in the FPT with the pivots, boundaries, and cells highlighted. Adapted from Kumar and Ramkrishna (1996a).

After defining the grid, Kumar and Ramkrishna (1996a) focused on the internal consistency of the method. The authors assured this characteristic by using a uniform discretisation, which provides internal consistency with regard to all the moments (Kumar and Ramkrishna, 1996a). This rationale allowed them to derive a discrete set of equations that describe the redistribution of particles whose sizes differ from the pivotal sizes (x_i) (Nopens, 2005). In practice, when a new particle of size v appears in the size range [x, x_{i+1}], formed due to aggregation or breakage, the method represents it by assigning fractions, *a* (v, x_i) and *b* (v, x_{i+1}), to the populations at x_i and x_{i+1}, respectively (Figure 3.5). For the consistency of two properties f_1 (v) and f_2 (v), these fractions must satisfy the following equations:

$$a(v, x_i)\, f_1(xi) + b(v, x_i)\, f_1(xi) = f_1(v) \tag{3.19}$$

$$a(v, x_i)\, f_2(xi) + b(v, x_i)\, f_2(xi) = f_2(v) \tag{3.20}$$

It should be noted that equations (3.19) and (3.20) can be generalised for the preservation of four moments by assigning a particle of size v to more than two pivots. Additionally, one is free to consider any two moments, not only just 0 (numbers) and 1 (mass). Hence, the population at representative point x_i gets a fractional particle for every particle that is born in size range [x_i, x_{i+1}] or [x_{i-1}, x_i] (Kumar et al., 2006; Kumar and Ramkrishna, 1996a).

Finally, Kumar and Ramkrishna (1996a) derived equations for aggregation and breakage. Due to the complexity of this process, the demonstrations for these equations are not shown in this thesis. For further reading, the reader is referred to Kumar and Ramkrishna (1996a). In spite of this, the main aspects of these derivations are presented because they are important for the understanding and characterisation of the overall method. The process of determining both the aggregation and breakage equations was independent of the choice of the grid. Besides that, the derivation is not associated with a specific aggregation/ breakage function, thus the FPT can be used for either binary or multiple aggregation or breakage events. Since the discretisation techniques used for both aggregation and breakage are based on a common strategy and involve the same variables, one can combine the equations in a

straightforward way to obtain discrete equations for simultaneous aggregation and breakage (Kumar and Ramkrishna, 1996a). Yet, as aforementioned, in this case only the coalescence phenomenon (which is part of the aggregation processes) was explored, thus the equation presented for the FPT only considers this process. Bearing all this information in mind, equation (3.21) can be written.

$$\frac{dN_i}{dt} = \sum_{\substack{j,k \\ x_{i-1} \leqslant (x_j + x_k) \leqslant x_{i+1}}}^{j \geqslant k} (1 - \frac{1}{2}\,\delta_{j,k})\,\eta\,\Gamma_{j,k}\,N_j\,N_k - N_i \sum_{k=1}^{M} \Gamma_{i,k}\,N_j \tag{3.21}$$

The first term represents the birth and the second one the death due to the coalescence process. As previously stated, N_i denotes the number concentration of particles in bin i and $\Gamma_{j,k}$ represents the coalescence frequency for sizes x_j, x_k. The remaining parameters are $\delta_{j,k}$ and η. The former is the Kronecker delta function, which assumes the value 0 when $x_j \neq x_k$ and 1 when $x_j = x_k$ (avoids counting coalescence events between bubble pairs twice). The latter - defined in equation (3.22) - guarantees the preservation of mass and numbers (solution of equations (3.19) and (3.20) when the two moments chosen to be conserved are 0 and 1).

$$\eta = \begin{cases} \frac{x_{i+1} - v}{x_{i+1} - x_i} & x_i \leq v \leq x_{i+1} \\ \frac{v - x_{i-1}]}{x_i - x_{i-1}} & x_{i-1} \leq v \leq x_i \end{cases} \tag{3.22}$$

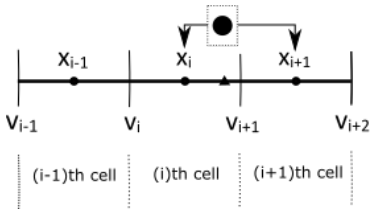

Figure 3.5: Schematic representation of the assignment of particles born in the ith cell, that do not coincide with an existing pivot, at the node x_i by the FPT. Adapted from Kumar et al. (2006); Nopens (2005).

3.4 Model formulation

With all the knowledge acquired from the previous sections, it is now possible to formulate the model. The focus is on the modifications made to the coalescence kernel and its insertion into the PBME.

3.4.1 Modifications to the coalescence kernel

In this work, the model proposed by Prince and Blanch (1990) was used to determine the coalescence frequency. This model is summarised in equation (3.23).

$$\Gamma_{j,k} = (\theta^{T}_{j,k} + \theta^{B}_{j,k} + \theta^{LS}_{j,k}) \times \lambda_{j,k} \tag{3.23}$$

Equation (3.23) illustrates the coalescence frequency term, where $\theta^{T}_{j,k}$, $\theta^{B}_{j,k}$, and $\theta^{LS}_{j,k}$ denote collisions due to turbulence, buoyancy, and laminar shear, respectively, while $\lambda_{j,k}$ represents the coalescence efficiency.

As stated in section 2.5.2.A, not all sources of collision are present in every system, because they strongly depend on operating conditions. In this case, collisions due to laminar shear were discarded. According to Prince and Blanch (1990), this type of collisions only occurs when the bubble column operates under high gas rates. In this situation, the bubbles tend to preferentially rise through the centre of the column, leading to the development of a gross circulation pattern, which generates a radial fluid velocity distribution. In turn, this promotes collisions between bubbles of the same size and rise velocity. This hydrodynamic regime is only observed when the bubble column operates with superficial gas velocities superior to 5 cm/s. As the maximum velocity in the experimentation process never surpassed this threshold, one can assume that collisions due to laminar shear did not take place. Therefore, the term $\theta^{LS}_{j,k}$ was removed and equation (3.24) obtained.

$$\Gamma_{j,k} = (\theta^{T}_{j,k} + \theta^{B}_{j,k}) \times \lambda_{j,k} \tag{3.24}$$

Further modifications to the coalescence efficiency were made, because it has been reported that this factor usually leads to overestimation of the coalescence frequency (Bhole et al., 2008; Chen et al., 2005; Laakkonen et al., 2007; Van Den Hengel et al., 2005). Chen et al. (2005) argues that this overestimation may arise from errors in the determination of the turbulent energy dissipation rate. On the other hand, Van Den Hengel et al. (2005) defends that the over-prediction is related to the arbitrary choice of the characteristic length. It is important to note the exponential dependence of the contact time (equation (3.17)) on both these parameters, which makes the model very sensitive to errors introduced by them. Van Den Hengel et al. (2005) also proposes that the rupture time is not disregarded when calculating

the coalescence time.

The approach of Van Den Hengel et al. (2005) to consider the rupture time is crucial to solve the over-estimation of the coalescence frequency. Coalescence efficiency reflects the probability that a collision results in coalescence and two times are involved in its calculation: coalescence time and contact time. For coalescence to take place, the contact time must be longer than the coalescence time. When the rupture time is considered, the coalescence time increases, leading to a decrease of the coalescence efficiency. Therefore, the over-prediction associated with the model developed by Prince and Blanch (1990) is mitigated.

When the rupture time is considered, the coalescence time corresponds to the sum of the drainage time and rupture time. The introduction of the rupture time allows the model to cope with the influence of the conditions of the gas-liquid interface, such as mobility, molecular interactions, and surfactant concentration, on the coalescence efficiency (Lee et al., 1987). Moreover, it strongly influences the size dependent part of coalescence efficiency, as the critical film thickness, which is highly affected by bubble size, is usually assumed to be a constant (Lee et al., 1987; Lo and Zhang, 2009).

Considering the findings of Van Den Hengel et al. (2005) and Chen et al. (2005), it was decided to decompose the coalescence time into drainage time and rupture time and discard the contact time expression proposed by Prince and Blanch (1990). Therefore, equation (3.24) was transformed into equation (3.25).

$$\Gamma_{j,k} = (\theta^{T}_{j,k} + \theta^{B}_{j,k}) \times exp(-\frac{t_{drainage\,j,k} + t_{rupture\,j,k}}{t_{contact\,j,k}}) \tag{3.25}$$

To determine the drainage time $t_{drainage\,j,k}$, the expression used was the one developed by Prince and Blanch (1990) (equation (3.15)). The rupture time, $t_{rupture\,j,k}$, and contact time, $t_{contact\,j,k}$, were determined by model calibration (explored in section 3.6). It is worth noting that the factors involved in these mathematical equations were found to be unknown. On the one hand, the influence of the conditions of the interface on coalescence efficiency was out of the scope of the experimental work performed by Amaral et al. (2018), thus the information needed to model this influence was not available. On the other hand, the expression that describes the contact time was deduced solely by dimensional analysis and it is only an approximation of the order of magnitude.

3.4.2 Insertion of the coalescence kernel into the PBME

The model that describes BSD dynamics in the system is given by equations (3.26) and (3.27). The former represents the discretised PBME obtained by the FPT, while the latter describes the coalescence frequency term presented in section 3.4.1. It is worth remembering that equation (3.26) can only be derived if one assumes perfectly mixed conditions and no bubble growth or nucleation.

$$\frac{dN_i}{dt}\,[\frac{1}{m^3_{fluid}\,\times\,s}] = \sum_{\substack{j,k \\ x_{i-1}\leqslant(x_j+x_k)\leqslant x_{i+1}}}^{j\geqslant k} (1-\frac{1}{2}\,\delta_{j,k}\,[-])\,\eta\,[-]\,\Gamma_{j,k}\,[\frac{m^3_{fluid}}{s}]\,N_j\,[\frac{1}{m^3_{fluid}}]\,N_k\,[\frac{1}{m^3_{fluid}}] - N_i\,[\frac{1}{m^3_{fluid}}]\sum_{k=1}^{M}\Gamma_{i,k}\,[\frac{m^3_{fluid}}{s}]\,N_j\,[\frac{1}{m^3_{fluid}}] \tag{3.26}$$

with

$$\Gamma_{j,k}\,[\frac{m^3_{bubble}}{s}] = (\theta^T_{j,k}\,[\frac{m^3_{bubble}}{s}] + \theta^B_{j,k}\,[\frac{m^3_{bubble}}{s}])\,\times\,\lambda_{j,k}\,[-] \tag{3.27}$$

In equation (3.26), N_i denotes the number concentration of bubbles in bin i, δ is the Kronecker delta function that avoids counting coalescence events between bubble pairs twice, and η is the factor proposed by Kumar and Ramkrishna (1996b), that guarantees the preservation of moments 0 (numbers) and 1 (volume). Equation (3.27) illustrates the coalescence frequency term for sizes j, k, where $\theta^T_{j,k}$ and $\theta^B_{j,k}$ denote collisions due to turbulence and buoyancy, respectively, while $\lambda_{j,k}$ represents the coalescence efficiency (expression derived in section 3.4.1).

To calculate BSD dynamics, equation (3.27) needs to be consistent with equation (3.26). As it is possible to see from the units of each term, they cannot be associated with each other. To understand how the coalescence frequency can be inserted into the PBME in a consistent manner, the physical meaning of each term present in equations (3.27) and (3.26) is crucial.

From the equations used to determine each term of equation (3.27) ($\theta^T_{j,k}$, $\theta^B_{j,k}$, and $\lambda_{j,k}$ see equation (3.5), (3.7), and (3.25), respectively), it is possible to infer that the resulting coalescence frequency corresponds to the volume of bubbles that is coalescing per unit time in a representative volume $[\frac{m^3_{bubble}}{s}]$. However, equation (3.26) requires this term to have units $[\frac{m^3_{fluid}}{s}]$. These units are derived by dimensional analysis. Equation (3.26) constitutes a balance of bubble concentration, changing over time due to the birth and death of bubbles. Clearly, the bubble concentration term - N - has units $[\frac{1}{m^3_{fluid}}]$, while δ and η have no units. Since bubble concentration is changing with time, the term on the left-hand side has units $[\frac{1}{m^3_{fluid}\times s}]$. For the units to be consistent, the coalescence frequency term must have units $[\frac{m^3_{fluid}}{s}]$. As such, equation (3.27) was modified to be consistent with equation (3.26). These modifications are presented in equation (3.28).

$$\Gamma_{j,k}\,[\frac{m^3_{fluid}}{s}] = V_{section}\,[m^3_{fluid}]\,\times\,\frac{((\theta^T_{j,k}+\theta^B_{j,k})\,\times\,\lambda_{j,k})\,[\frac{m^3_{bubble}}{s}]}{(v_j+v_k)\,[m^3_{bubble}]} \tag{3.28}$$

Here, the coalescence frequency is divided by the volume of the bubble created in the coalescence event and multiplied by the volume of the fluid where the coalescence process is taking place. The

former operation transforms the volume of bubbles coalescing per unit time in a unit volume into the number of coalescence events per unit time occurring in a unit volume $[\frac{1}{s}]$. The latter produces the number of coalescence events per unit time taking place in the volume considered $[\frac{m^3 fluid}{s}]$. These considerations allow the resulting coalescence frequency, denoted by equation (3.28), to be consistent with equation (3.26).

Equations (3.26) and (3.28) represent the model developed to predict BSD dynamics. These equations were implemented in MATLAB® and solved with the classical Runge-Kutta method.

3.5 Model inputs

At this point, the inputs needed by the developed model can be presented. The focus is on the definition of the grid, required by the FPT, as well as the initial condition, that must be supplemented to the PBME.

3.5.1 Grid definition

As described in section 3.3.4.B, the grid used by the FPT consists of boundaries and pivots. To develop the grid used by the model, two steps were followed: (1) definition of a diameter based grid and (2) transformation of the diameter grid into a volume based one. The boundaries of the first ranged from 0.1 mm to 5.9 mm and the distance between boundaries was 0.2 mm. The pivots were defined as the middle points between consecutive boundaries. For the volume grid, the volume of the equivalent sphere to each diameter was calculated.

Even though only the volume based grid was used in model calculations, the first step was essential to facilitate the comparison between experimental and model results. The diameter based grid describes the bins used to derive the experimental BSD. As the grid used by the model was obtained by transforming this grid, simulation results can be easily converted and represented in the diameter grid. The second step was necessary to correctly describe the coalescence phenomenon. When two bubbles coalesce, the diameter of the resulting bubble does not strictly correspond to the sum of both diameters. In fact, the property that is preserved is mass, since the mass of the resulting bubble is the sum of the two masses coalesced. However, the gas is deemed to behave as ideal, thus volumes can also be assumed to be additive. Since it is more practical to use volume as the internal coordinate of the PBME, volume was used to describe coalescence. Figure 3.6 displays the initial sections of both grids and the relationship between them.

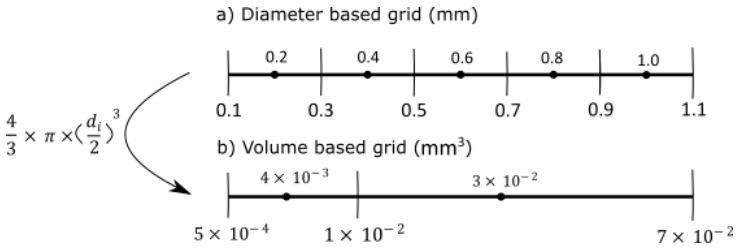

Figure 3.6: Grids used in this work: a) diameter based grid (mm) and b) volume based grid (mm^3). The equation that allows the transformation of grid a) into b) is highlighted.

3.5.2 Initial condition

The model needs to be supplemented with an initial condition, which corresponds to the distribution of number concentration in the system at time zero. As the initial distribution is observed right above the diffuser, the focus is only the first section of the column. The determination of the initial distribution can be done by following the steps: (1) determination of both the volume and gas holdup of the first section; (2) transformation of the measured diameter based BSD into a volume based BSD (the procedure is the same as the one presented in section 3.5.1); (3) determination of the gas holdup in each bin according to the volume based BSD (since the grid is different, the distribution changes); (4) calculation of the number of bubbles in each bin by dividing the gas holdup by the representative volume of the bin; (5) calculation of the total number of bubbles and bubble concentration; and (6) definition of the initial condition by calculating the bubble concentration in each bin using the experimentally determined diameter based BSD.

In practice, the model is only supplemented with the total number of bubbles calculated at step (5), as the experimental BSD and volume of the section for the studied system are known. The values are summarised in Table 3.1.

Table 3.1: Total number of bubbles for each solution and airflow rate.

Solution	Airflow rate [L/min]	Number of bubbles ($\times 10^4$)
CW	2	1.86
	4	3.14
	6	3.92
	8	5.75
XG0.2	2	1.74
	4	2.53
	6	2.62
	8	3.24
XG0.8	2	0.89
	4	1.23
	6	1.68
	8	2.22

3.6 Model calibration and validation

Model calibration is a critical step of the modelling exercise, since an uncalibrated model cannot be used in practical applications. The goal of this procedure is to estimate unique parameter values which lead to a good agreement between the model predictions and the experimental data (Van Daele, 2016). According to Makinia (2010), there are three ways to calibrate a model: (1) by deriving parameters, that are fundamental in nature, from theoretical considerations; (2) by using experiences with the particular model that have been acquired in similar applications; and (3) by adjusting model coefficients to match the results of experiments. In this work, the latter methodology was followed, since reliable experimental data of the system pretended to be modelled was available (the conducted experiments were already described in section 3.2).

After the calibrated model is obtained, it is possible to proceed to the validation step. This step consists in comparing the simulation results predicted by the calibrated model with an independent experimental data set, i.e. other than the one used in the calibration step (Makinia, 2010).

3.6.1 Calibration and validation procedure

As previously mentioned in section 3.6, the calibration process consisted in adjusting the model coefficients to match the experimental results. To obtain this set of parameters, there was a need to quantify the fit between the model prediction and experimental data, thus the use of mathematical tools was crucial. In this case, a nonlinear optimisation approach, which evaluates the offset between the model and experimental data using an objective function, was used. This approach finds the optimal parameter set, $\hat{\phi}$, by minimising the objective function, $J(\phi)$ (equation (3.23)) (Van Daele, 2016).

$$\hat{\phi} = arg \underset{\phi \in \Phi}{min} J(\phi) \tag{3.29}$$

In equation (3.23), ϕ is the np-dimensional vector of model parameters (np represents the number of model parameters) and Φ the np-dimensional vector of possible model parameters.

There are numerous objective functions, but usually the one used is the weighed sum of squared errors (WSSE), denoted in equation (3.24) (Donckels, 2009; Van Daele, 2016).

$$J(\phi) = \sum_{j=1}^{H} \sum_{i=1}^{M} (y_{ij} - \hat{y}_{ij}(\phi))' \,.\, A \,.\, (y_{ij} - \hat{y}_{ij}(\phi)) \tag{3.30}$$

Here, H is the number of heights studied, M is the number of experimental measurements per height, y represents the nm-dimensional vector of measured response variables (nm represents the number of measured state variables), $\hat{y}$ denotes the nm-dimensional vector of predicted response variables, and

A is the nm-dimensional matrix, which contains the weighing coefficients (Donckels, 2009; Van Daele, 2016). Although this matrix is often considered as the inverse of the measurement covariance matrix (Donckels, 2009), in this thesis it will always be considered as the unity matrix I_{nm}. It is worth noting that by discarding the influence of A, one is assuming that all experimental measurements have the same importance in the calibration process. This simplification is supported on the fact that both the model structure and experimental data are assumed to be reliable. Hence, the value of $J(\phi)$ will approach zero when $\hat{\phi}$ is determined.

Now that the objective function has been defined, it is important to discuss the optimisation method used to obtain the optimal parameter set, $\hat{\theta}$. In this case, the optimisation algorithm used was the SIMPLEX search method implemented in the function *fminsearch* provided by MATLAB®, which searches for the minimum of a defined function. This specific function is a local optimisation algorithm, since the search is restricted to the neighbourhood of an initial guess in the parameter set space that must be provided. This type of algorithm is highly dependent on the initial guess, since the found value can vary with it. This disadvantage is more pronounced when the objective function has multiple local minima (Donckels, 2009). Global optimisation algorithms could have been used, but these methods are computationally more demanding.

In this thesis, the data set corresponding to the top section of the bubble column (120 cm) was used to calibrate the model. The calibration step was done for each solution and airflow rate. Only two parameters were calibrated: rupture time and contact time, as the factors involved in the mathematical expressions were found to be unknown. Twelve values were determined for each parameter, since these parameters vary with airflow rate and liquid viscosity. Therefore, twelve different expressions (represented by equations (3.26) and (3.28)) were obtained, one for each airflow rate and solution.

To validate the model, the experimental BSD measured for 20, 40, 60, 80, and 100 cm was used. Each expression was only validated for the solution and airflow rate used in the calibration step, e.g. the calibrated model obtained for CW 2 L/min was validated with the experimental BSD measured under the same conditions.

4

Results and discussion

Contents

In this chapter, the model developed in chapter 3 is applied to the system studied by Amaral et al. (2018). First, the strategy used to compare simulation and experimental results is explained. Secondly, the results of the calibration process are analysed and discussed. The chapter ends with the analysis of the validation process.

4.1 Simulation time to column height correspondence

To compare simulation and experimental results, it is necessary to associate the simulation time with the height of the column. This necessity arises from the fact that the model predicts BSD over time, yet measurements were made along the height of the column. To accomplish this, the rising velocity of the bubbles was determined. As considered in section 3.1, bubbles rise through the bubble column at a constant terminal rising velocity. This velocity can be calculated with equations (3.9), (3.10), and (3.11) by knowing the diameter of the bubble. As there is not a unique bubble size, but rather a distribution, the average size was considered. This average was determined for each section (5 to 120 cm) and then averaged again, so that an average bubble diameter for the entire column could be determined. These calculations introduce an error in the computation of the terminal rising velocity, because there is no linear relationship between this variable and bubble diameter. Once the terminal rising velocity was calculated, the time that the bubbles take to climb each section could be evaluated, since the height of each section is known. In Table 4.1, the average bubble diameter for each solution and airflow rate and the terminal rising velocity calculated by equations (3.9), (3.10), and (3.11) are summarised.

Table 4.1: Average of the bubble diameter for the entire column and respective bubble terminal rising velocity for each solution and airflow rate.

Solution	Airflow rate [L/min]	Average bubble diameter [mm]	Terminal rising velocity [m/s]
CW	2	1.24	0.34
	4	1.38	0.33
	6	1.42	0.32
	8	1.44	0.32
XG0.2	2	1.44	0.28
	4	1.53	0.29
	6	1.65	0.29
	8	1.70	0.28
XG0.8	2	1.77	0.19
	4	1.74	0.19
	6	1.68	0.18
	8	1.64	0.18

4.2 Model calibration

Due to the high number of operating conditions studied, only the results for airflow rates of 2 and 8 L/min are presented. The results for CW, XG0.2, and XG0.8 are displayed in Figures 4.1, 4.2, and 4.3, respectively.

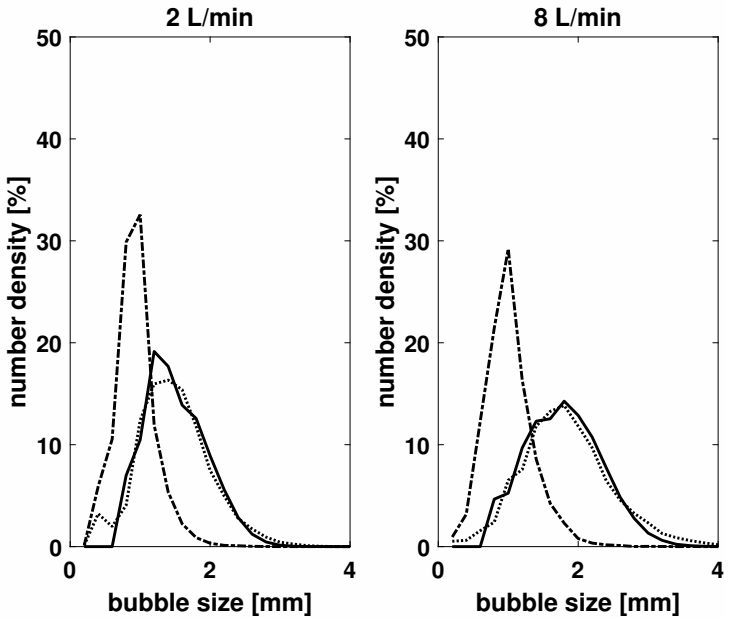

Figure 4.1: Experimental BSD for tap water (grey dash-dot line - at 5 cm from diffuser; grey dotted line - at 120 cm from diffuser) and calibrated BSD (black line - at 120 cm from diffuser).

The effect of airflow rate on BSD in CW can be studied by comparing the experimental distributions. After analysing Figure 4.1, one can observe a shift to larger bubbles at a higher airflow rate. An increased airflow rate enables a larger volume of gas to enter the system, which translates into a higher gas holdup value. This raises the number of bubbles and introduces more turbulence, which in turn increases collisions between bubbles, making successful coalescence events more likely to occur. Since the reason for growth along the height of the column is coalescence, it follows that bubbles grow more at increased airflow rates. In a similar way, Figure 4.2 depicts a shift to larger bubbles at a higher airflow rate. This was expected, since the rationale presented to justify this behaviour in CW also holds for XG0.2.

In Figure 4.3, the shift to larger bubbles is not clear. In fact, measurements show that bubbles do not grow along the height of the column at an airflow rate of 8 L/min. As stated by Amaral et al. (2018), the reason for this observation is unclear, as it was expected that bubbles would grow along the height of the column due to coalescence.

The effect of liquid viscosity on BSD can also be assessed through the analysis of Figures 4.1 and 4.2. The comparison of the measured BSDs leads to one conclusion: a higher liquid viscosity reduces

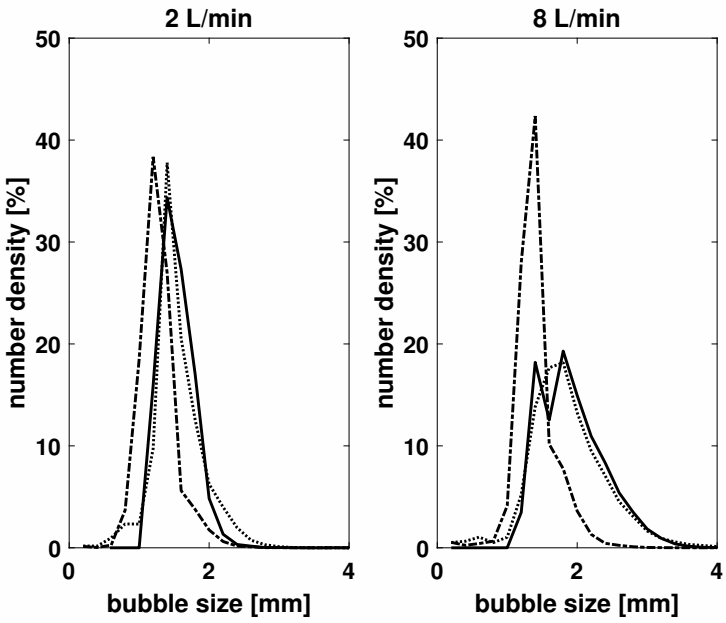

Figure 4.2: Experimental BSD for XG0.2 (grey dash-dot line - at 5 cm from diffuser; grey dotted line - at 120 cm from diffuser) and calibrated BSD (black line - at 120 cm from diffuser).

growth along the height of the column. By analysing the grey dotted lines in Figures 4.1 and 4.2, it is possible to observe that the shift to larger bubbles is less pronounced in XG0.2. As previously stated, bubbles grow along the height of the column due to coalescence, which is more prevalent when the number of collisions increases. If the liquid is more viscous, the movement of bubbles through the fluid is impaired. Hence, the number of collisions diminishes, leading to fewer coalescence events. Once again, this behaviour is not clear in Figure 4.3.

The sum of squared errors (SSE) enables the evaluation of the calibration process, since its value quantifies the fit between experimental and calibration results. When the value of SSE approaches zero, the calibration and experimental curves overlap, and thus the model is adequately calibrated. The values determined in the calibration process for each solution and airflow rate are summarised in Table 4.2.

Table 4.2: Values of SSE obtained in the calibration process for each solution and airflow rate.

Solution	Airflow rate [L/min]	SSE
CW	2	45
	8	22
XG0.2	2	143
	8	60
XG0.8	2	682
	8	529

The calibration process produced better results for CW and XG0.2 than for XG0.8. Two observations support this conclusion: (1) the SSE values presented in Table 4.2 for CW and XG0.2 are considerably

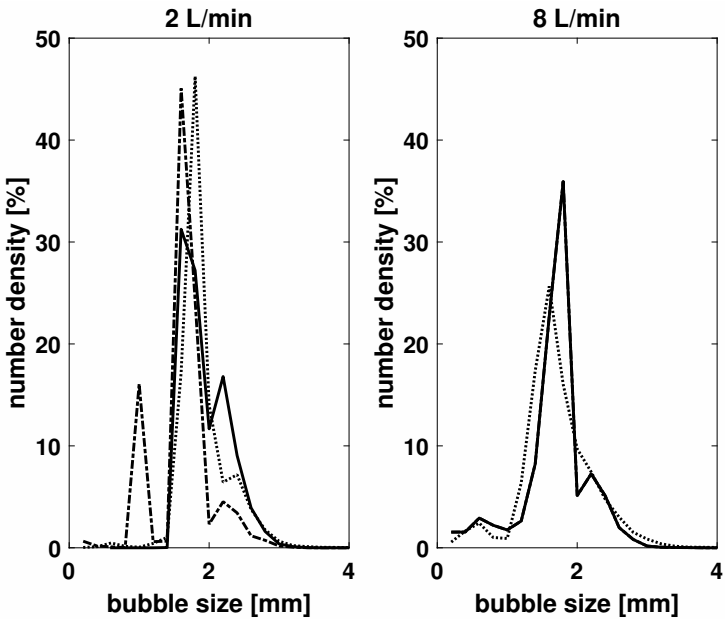

Figure 4.3: Experimental BSD for XG0.8 obtained in the two repeated experiments (grey dash-dot line - at 5 cm from diffuser; grey dotted line - at 120 cm from diffuser) and calibrated BSD (black line - at 120 cm from diffuser).

lower than those determined for XG0.8 and (2) the calibrated BSD curve (black lines) and experimental BSD curve at 120 cm from diffuser (grey dotted lines) are similar for CW and XG0.2, whereas for XG0.8 they are different. The discrepancies observed are related to the model and experimental process.

As stated in section 3.4.1, the model developed is a modification of the expression proposed by Prince and Blanch (1990). The modifications made to the original model are mainly associated with the coalescence efficiency term, since it has been reported that this term is the cause for the over-prediction associated with the model of these authors (Bhole et al., 2008; Chen et al., 2005; Laakkonen et al., 2007; Van Den Hengel et al., 2005). According to the experimental observations, the effect of liquid viscosity is crucial because it strongly influences the amount of collisions, thus affecting the coalescence phenomenon. The effect of liquid viscosity was considered, as the calibrated parameters could be freely modified. Consequently, the errors introduced by changes in liquid viscosity were implicitly corrected by these parameters. The model is then able to cope with changes in liquid viscosity, which can be seen in Figures 4.1, 4.2, and 4.3. Nonetheless, the effect of liquid viscosity should be explicitly considered. Since the influence of this parameter was not completely described, the misfit between model and experimental results can be partially related to the model formulated. Due to the complexity of all phenomena and parameters described by the model, this idea is further explored in section 4.2.1.

Another plausible justification for the observations made for XG0.8 is associated with the experimental process. As previously stated, Amaral et al. (2018) observed an unexpected behaviour for XG0.8 8 L/min. Although the author did not provide an explicit justification, it mentioned that further research

would be conducted to explain this observation. Helser (2018) repeated the experiment performed for XG0.8 two more times. This decision arose from the fact that, in the specific case of XG0.8, the solution becomes opaque, hindering the identification of the bubbles by the digital image analysis used. It should be noted that the experimental procedure used was the one described in section 3.2. The calibration results obtained were similar to one another and are depicted in Figure 4.4. In Table 4.3, the SSE is presented. To distinguish the repeated experiments, the solution is referred to as XG0.8*.

Table 4.3: Values of SSE obtained in the calibration process for the repeated experiments in XG0.8*.

Solution	Airflow rate [L/min]	SSE
XG0.8*	2	302
	8	109

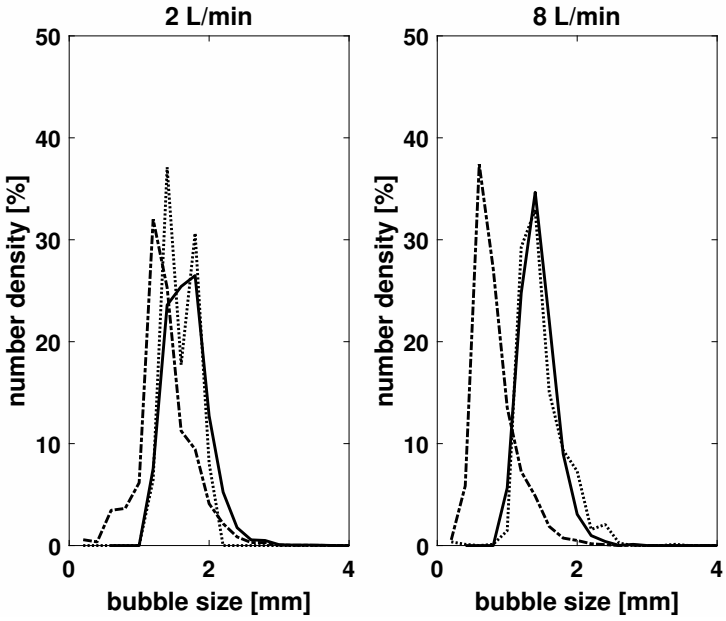

Figure 4.4: Experimental BSD for XG0.8* (grey dash-dot line - at 5 cm from diffuser; grey dotted line - at 120 cm from diffuser) and calibrated BSD (black line - at 120 cm from diffuser).

In this case, the curves are similar and the SSE values are significantly lower than the ones determined for XG0.8 presented in Table 4.3. This leads to the conclusion that this hypothesis is a significant contributor for the misfit between model and experimental results. The results considered henceforth are the ones presented in Figure 4.4 and denoted by XG0.8*.

4.2.1 Analysis of the parameters obtained by model calibration

Now that the graphs have been studied, the values of the calibrated parameters must be addressed. The values of rupture and contact times for all conditions are presented in Table 4.4.

Table 4.4: Values of rupture and contact times determined by the calibration process for each solution and airflow rate.

Solution	Airflow rate [L/min]	Rupture time [$\times 10^{-3}$ s]	Contact time [$\times 10^{-3}$ s]
CW	2	27	2.1
	4	38	2.9
	6	78	5.6
	8	79	5.6
XG0.2	2	1.8	0.23
	4	4.2	0.40
	6	35	2.6
	8	57	4.2
XG0.8*	2	1.4	0.20
	4	1.7	0.21
	6	2.0	0.20
	8	2.2	0.20

By analysing Table 4.4, it is possible to see that both rupture and contact times increase with the airflow rate for CW and XG0.2. For XG0.8*, the rupture time increases, but the contact time does not appear to follow a trend. On the other hand, both rupture and contact times appear to decrease when liquid viscosity increases.

To understand the influence of airflow rate and liquid viscosity on the rupture and contact times, the physical meaning of the coalescence efficiency term is essential. This term reflects the probability that a collision results in coalescence and it is composed of two parameters: coalescence time and contact time. The first is the time required for bubbles to coalesce, while the second refers to the time that bubbles interact with each other. In this work, the coalescence time was decomposed into drainage time and rupture time. The former accounts for the time needed for the liquid film to reach a critical thickness, while the latter is the time required for the liquid film to break. For coalescence to happen, the contact time must be longer than the coalescence time.

As it is possible to observe in Table 4.4, the rupture time is higher than the contact time in every condition. The coalescence time is not equal to the rupture time but to the sum of the rupture and drainage times. As the drainage time cannot assume a negative value, the calculated coalescence time is always higher than the computed contact time. Therefore, it would appear that coalescence should not occur in the system. However, one must not forget that: (1) the values presented in Table 4.4 represent mean values and (2) the coalescence efficiency term is statistical in nature. Even though the coalescence time on average is higher than the contact time, this does not mean that this relationship holds for every collision. In some cases, the coalescence time is lower than the contact time, allowing

coalescence to occur. In fact, the analysis of Figures 4.1, 4.2, 4.3, and 4.4 leads to the conclusion that the model can adequately predict coalescence, as a shift to larger bubbles is observed.

From the comparison of the average values of rupture time and contact time, one can only infer that most collisions do not result in coalescence. This conclusion is in line with what has been reported about the model developed by Prince and Blanch (1990) (Bhole et al., 2008; Chen et al., 2005; Laakkonen et al., 2007; Van Den Hengel et al., 2005): the coalescence efficiency term is the reason for the overestimation of coalescence frequency. The calibrated parameters obtained support this observation. If the rupture time is not considered in the determination of the coalescence time, as suggested by Prince and Blanch (1990), the coalescence efficiency increases. Hence, the overestimation of coalescence frequency would be even larger.

The effect of a change in airflow rate can be associated with bubble size, as a shift to larger bubbles is more pronounced at higher airflow rates. In turn, according to Lee et al. (1987), one of the key properties related to coalescence efficiency is bubble size. Therefore, the influence of the airflow rate on rupture and contact times can be addressed by studying the variations in bubble size. When bubbles are bigger, the drainage and contact times are larger. The drainage time increases, since a larger amount of liquid trapped between the bubbles must be drained (Kim and Lee, 1987; Lo and Zhang, 2009). The liquid film that needs to be ruptured for coalescence to occur is larger and, thus, the rupture time also increases. The contact time increases because bigger bubbles are harder to be separated. In a turbulent flow, there are turbulent eddies that communicate energy to the bubbles. When the energy communicated by the eddy is large enough, the bubbles are separated. If the bubbles are bigger, the energy needed to separate them increases and, as such, the probability of separation decreases (Lee et al., 1987). Thus, a higher airflow rate leads to an increase in the drainage, rupture, and contact times. This is observed in Table 4.4, since both rupture and contact times increase with airflow rate. The only exception is the contact time for XG0.8*, which can be related to the fact that bubbles grow less in this solution, making the variation in rupture time and contact time nearly inexistent.

Even though the trend observed for both rupture and contact times has been justified, the effect of an increasing airflow rate on coalescence efficiency is not straightforward. For coalescence to occur, the bubbles need to remain in contact for sufficient time to allow the film drainage and rupture processes to take place. If the contact time increases, the probability of a successful coalescence event is higher, as the film drainage and rupture processes have more time to occur. Conversely, if the drainage and rupture times increase, the probability of a successful coalescence event diminishes. Therefore, it is possible to conclude that an increase or decrease of coalescence efficiency depends on the trade-off between the coalescence time (drainage time plus rupture time) and contact time. Adding to this, the size dependence of each parameter greatly influences the coalescence efficiency. The drainage time depends on bubble size (see equation (3.15)). As stated in section 3.4.1, the rupture time was intro-

duced to capture the strong size dependence of coalescence efficiency on the critical film thickness and conditions of the interface. Despite being discarded, equation (3.17) gives an idea of the size dependence of the contact time, which is considerably lower than the other two. Thus, variations in bubble size change each parameter in different ways. This also contributes to the complexity of assessing the effect of an increasing airflow rate on coalescence efficiency.

The effect of liquid viscosity on these parameters is hard to evaluate, due to limitations of the model. On the one hand, the continuous phase viscosity should influence the turbulent collision frequency, since it was observed that this variable hampers turbulence. The turbulent collision rate (equation (3.5)) is not accounting for this effect, because no parameter is influenced by it. To the author's best knowledge, no turbulent collision rate expression considering this influence has been implemented in coalescence kernels reported in the literature. However, in the author's opinion, equation (3.15) should explicitly consider this.

On the other hand, viscosity would be expected to affect the drainage time. Equation (3.15), used to determine it, assumes that the liquid is inviscid and, as such, film drainage is completely inertial (Lee et al., 1987). For viscous liquids, equation (3.15) must be modified, as the film surfaces become partially immobile. It is worth noting that inertial and viscous forces are always present in the motion of a fluid. Inertial forces are related to the momentum of the fluid, whereas viscous forces are associated with the fluid's resistance to movement. When liquid viscosity increases, the viscous forces become more relevant, increasing the film surface immobility. In this case, the film must be expelled by laminar flow, which greatly increases the drainage time (Lee et al., 1987). Once again, this influence of liquid viscosity on drainage time is not explicitly considered.

Although the model does not directly consider the effect of viscosity on both turbulent collision rate and drainage time, the modifications made to the model developed by Prince and Blanch (1990) enable it to account for them. This is proven by the results shown in Figures 4.1, 4.2, and 4.4 since the model can describe BSD in all the solutions studied. The parameters that are considering the influence of liquid viscosity on BSD are the rupture and contact times, because they were used to calibrate the model. Hence, the errors caused by changes in liquid viscosity are compensated by the combination of values found in the calibration process. The drawback of this strategy is that calibrated parameters tend to lose their physical meaning, due to the assumptions used to formulate the model. Theoretically, if all other factors are kept equal, both rupture and contact times should increase with liquid viscosity (Lee et al., 1987). The first because a more viscous film takes more time to break than a free liquid film. The second because viscosity hampers coalescence and, as such, turbulent eddies communicate less energy to bubbles, which in turn diminishes the probability that two bubbles are separated. This trend is not observed, as the assumptions are encompassed in the values found for these variables.

Despite its limitations, the model is well calibrated for every operating condition and solution tested.

One can then conclude that the model is adequately describing the system BSD dynamics. Two main arguments support this observation: (1) the values of the calibrated parameters are reasonable and (2) the model can cope with unexpected errors.

In the case of water, the calibrated values for rupture and contact times are expected to be almost identical to the ones of the actual physical parameters, since the considerations used to develop equations (3.5) and (3.15) hold true. The values obtained for the XG solutions can be compared to these ones to assess their veracity. Although the effect of viscosity was not properly addressed in the turbulent collision frequency and drainage time, the computed parameters for XG solutions are close to the order of magnitude of the ones calculated for water. This proves that the parameters used for calibration allow the model to cope with the errors introduced by the assumptions, without significantly jeopardising their physical interpretation.

Even though the experimental data is most likely corrupted, the model is able to predict a reasonable BSD (Figure 4.3). In addition, the conditions of the interface, which has been reported to have a strong influence on coalescence efficiency, were not properly explored. As stated in section 3.4.2, this was not in the scope of the experimental work performed by Amaral et al. (2018), thus its influence could not be properly modelled. It is expected that numerous species that influence the characteristics of the interface are present, as either CW or XG are not pure liquids. Nonetheless, the model can deal with these errors, hence reinforcing the idea that the model accounts for errors introduced by unexpected sources.

4.3 Model validation

To validate the model, the behaviour of the model was compared to the one measured in the experimental process. The data collected at the bottom and top of the column were not used, since the former corresponds to the initial condition and the latter was used to calibrate the model. Due to the high number of experimental measurements, only the ones made at 20, 60, and 100 cm are shown. The SSE can be used to assess the validation process, thus they are also analysed in this section.

4.3.1 CW results

The values of SSE obtained in the validation process for CW are presented in Table 4.5. The validation results are presented in Figure 4.5.

Table 4.5: Values of SSE obtained in the validation process for CW.

Airflow rate [L/min]	Heights [cm]	SSE
2	20	254
	60	81
	100	54
8	20	124
	60	53
	100	36

By analysing Figure 4.5, one can observe a shift to large bubbles along the height of the column, which can be attributed to coalescence. Moreover, the model is accurately predicting BSD along the height of the system, as the curves are similar.

The values in Table 4.5 show that the fit between model and experimental results is better for 60 and 100 cm than for 20 cm. The reason for this can be related to the calibration process. The data set used to calibrate the model was the one corresponding to the top of the column, i.e. the BSD measured at 120 cm. Since BSD changes along the height of the column, the BSD measured at 20 cm is the most different one from the BSD measured at 120 cm. Therefore, the deviations between model and experimental results increase.

Another conclusion can be drawn from the analysis of Table 4.5: model predictions are better for a higher airflow rate. This can be related to the over prediction associated with the model developed by Prince and Blanch (1990), which was the basis of the model formulated in this work. Even though modifications were made to mitigate this effect, it is possible that it still bears some influence on the final predictions. It is worth noting that the modifications only addressed the coalescence efficiency term, thus possible errors introduced by the collision frequency term were not explicitly corrected. In fact, one can observe in Figure 4.5 that the model tends to overestimates BSD along the height of the system.

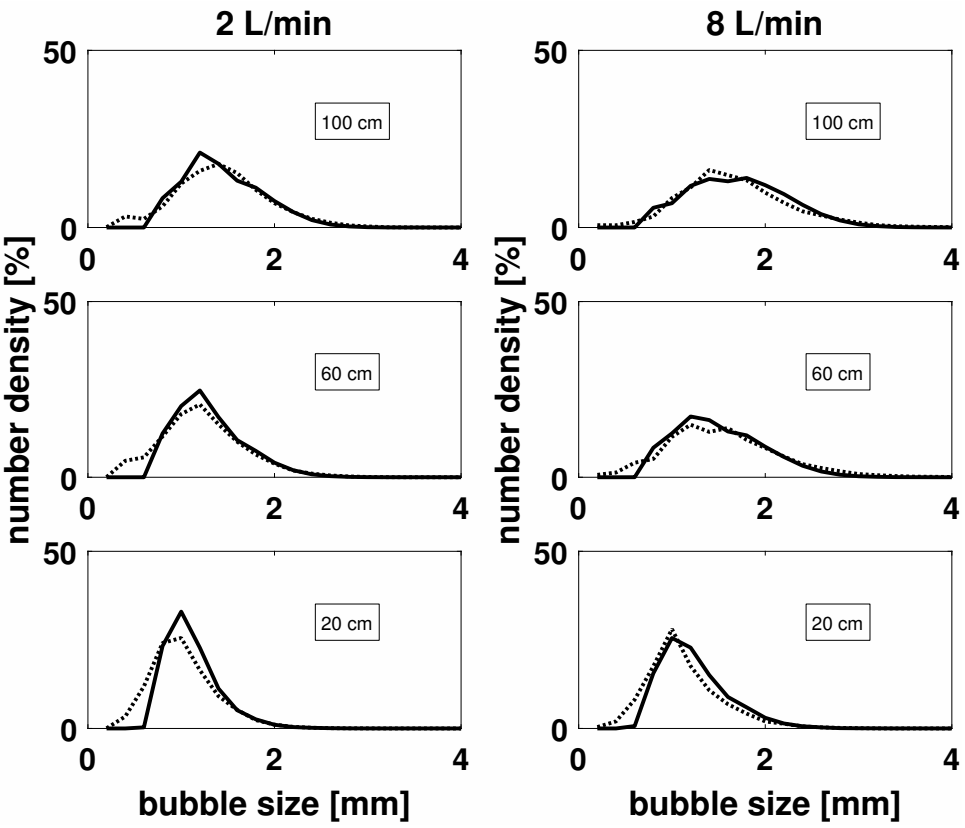

Figure 4.5: Experimental BSD for CW (grey dotted line) and BSD predicted by the model (black line).

Despite these two observations, the model is having a very good performance, which leads to the conclusion that it can predict BSD dynamics in CW.

4.3.2 XG0.2 results

In Table 4.6, the SSE values determined in the validation process for XG0.2 are presented. In Figure 4.6, the validation results for XG0.2 are displayed.

Table 4.6: Values of SSE obtained in the validation process for XG0.2.

Airflow rate [L/min]	Heights [cm]	SSE
2	20	40
	60	227
	100	192
8	20	33
	60	98
	100	44

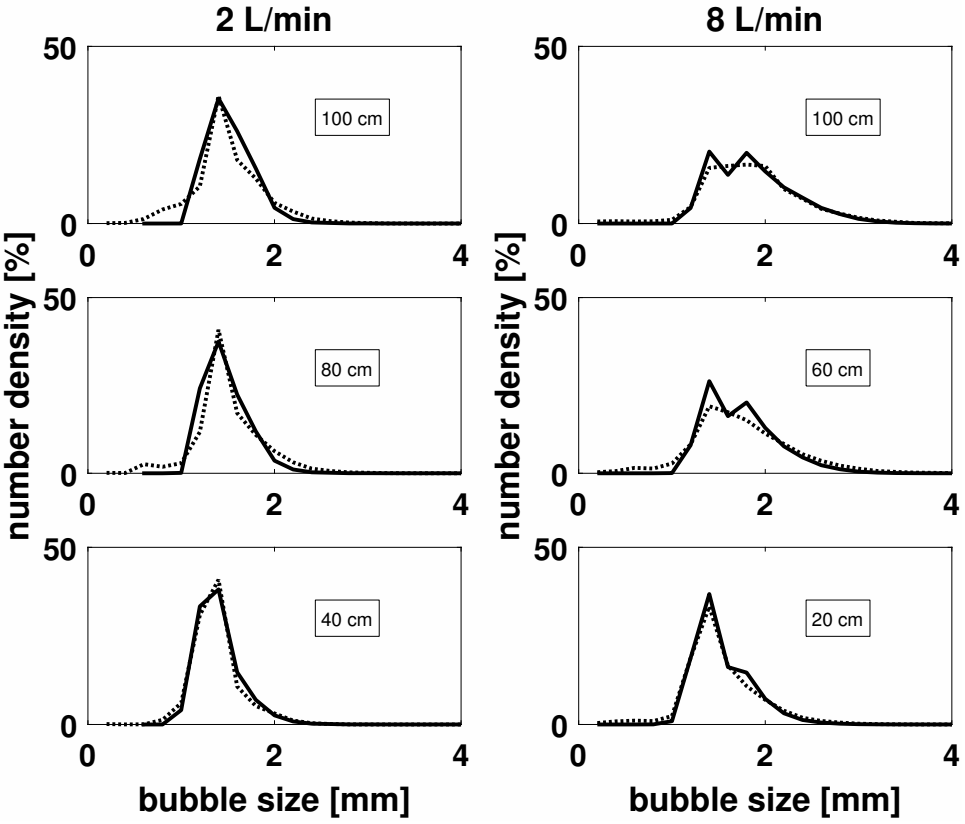

Figure 4.6: Experimental BSD for XG0.2 (grey dotted line) and BSD predicted by the model (black line).

Once again, one can observe a shift to larger bubbles along the height of the column due to coalescence. In addition, the effect of increasing liquid viscosity on BSD is evident, as the bubbles grow less than the ones in CW (see Figure 4.5). The model accurately predicts BSD dynamics along the height of the column, as the experimental and model curves are similar. As the SSE values corresponding to 2L/min are higher than the values calculated for 8 L/min, the model does not perform as well for this

airflow rate (see Table 4.6).

As previously stated, the model that served as basis for the model developed in this dissertation tends to over predict coalescence frequency values, leading to a shift to larger bubbles. By analysing Figure 4.6, one can verify that the model constantly over predicts BSD along the height of the bubble column. This behaviour is more explicit at a lower airflow rate, since bubbles grow less and, as such, the deviations between experimental and model results are bigger. This observation supports the argumentation made for CW, as the performance of the model is very similar.

On the other hand, the misfit between experimental and model results is larger for 60 and 100 cm than for 20 cm, which was not observed in CW. According to Amaral et al. (2018), liquid viscosity hampers coalescence further away from the diffuser, thus there are fewer coalescence events in 60 and 100 cm than in 20 cm. As the model overestimates coalescence frequency, the discrepancies between model and experimental results increase at higher heights.

Although there are some deviations between model and experimental results, the model is accurately predicting BSD dynamics in XG0.2.

4.3.3 XG0.8* results

The SSE values calculated in the validation process of XG0.8* are indicated in Table 4.7. The validation results for XG0.8* are illustrated in Figure 4.7.

Table 4.7: Values of SSE obtained in the validation process for XG0.8*.

Airflow rate [L/min]	Heights [cm]	SSE
2	20	181
	60	229
	100	985
8	20	1286
	60	397
	100	500

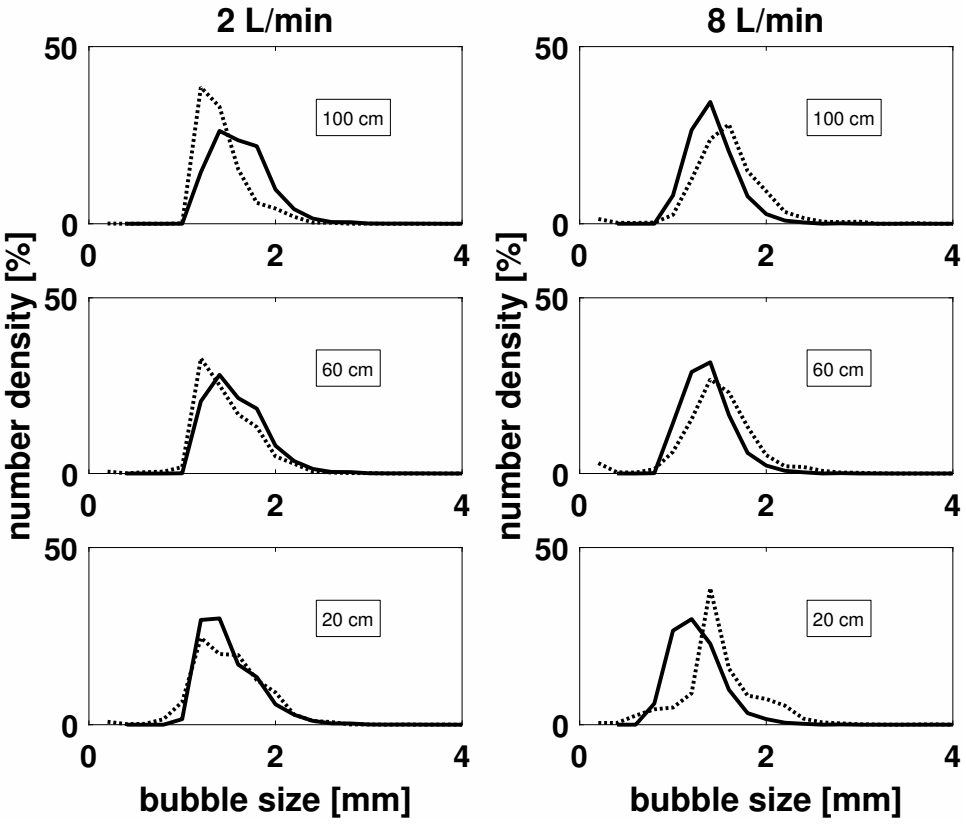

Figure 4.7: Experimental BSD for XG0.8* (grey dotted line) and BSD predicted by the model (black line).

The observations of the experimental BSDs made for CW and XG0.2 hold for XG0.8*, which confirms that: (1) a higher airflow rate leads to a shift to larger bubbles and (2) liquid viscosity hampers coalescence and, as such, the growth of bubbles due to coalescence is less pronounced when this variable increases. Conversely, the performance of the model in XG0.8* is different from the one in CW and XG0.2, as it is confirmed by the SSE values presented in Table 4.7, which are significantly larger than

the ones shown in Tables 4.5 and 4.6.

When looking at the experimental results measured at 2 L/min, one can observe that the growth along the height of the column is almost inexistent. On the one hand, the misfit between model and experimental results can be related to the corruption of experimental data. As previously stated, the BSDs measured in XG0.8 by Amaral et al. (2018) (see Figure 4.3) showed an unexpected behaviour and, as such, were discarded. Although the results depicted in Figure 4.6 do not show the same trends, it is possible to verify that the growth of bubbles is not concordant with the one observed in CW and XG0.2. On the other hand, the fact that the influence of liquid viscosity was not explicitly modelled introduces errors in the model, making it lose part of its predictive capability for more viscous solutions. In addition, the influence of conditions of the interface can also be affecting model predictions. Therefore, the discrepancies observed can be associated with experimental data corruption and model formulation. Even though the disparity between model and experimental results is more pronounced in XG0.8*, the model has an adequate performance.

In conclusion, the model can predict BSD dynamics in every case.

5

Conclusions and future perspectives

Contents

5.1 Conclusions

Through an extensive literature review, the current knowledge gaps in the field of oxygen transfer modelling were identified. On one hand, the assumption of well-mixed conditions was pinpointed as a limitation in the description of oxygen transfer, as it does not accurately describe the DO profile observed in practice. On the other hand, the estimation of BSD in the determination of OTR was found to be crucial. The latter was the focus of this work.

The BSD dynamics observed by Amaral et al. (2018) were successfully described using the PBM framework in conjunction with a coalescence model. Modifications to the basic form of this model were introduced to consider important effects on BSD, namely viscosity and conditions of the interface, such as mobility, molecular interactions, and surfactant concentration. In addition, the coupling strategy implemented to guarantee consistency between the PBM framework and the developed coalescence kernel was described and explained. Thus, this work can be a useful source to comprehend PBM and the underlying physical phenomena involved in the coalescence process.

The model was implemented in MATLAB® and solved with the classical Runge-Kutta method. The SSE objective function and a local optimisation algorithm were used to calibrate the model. The two calibrated parameters were the rupture and contact times, since the factors involved in the determination of these factors were found to be unknown. Finally, the model was validated, leading to the conclusion that it can be used to accurately predict BSD dynamics in the system studied by Amaral et al. (2018).

The formulation of the developed model produced valuable insights on the limitations of current coalescence modelling approaches. The coalescence models reported in the literature lack robustness and do not consider numerous effects on BSD, which were identified as key to correctly describe the phenomenon. The impact of critical film thickness on coalescence time should not be ignored, as this parameter strongly depends on bubble size and conditions of the interface. Moreover, the determination of a contact time based on dimensional analysis should be avoided. Even though the model formulated addresses these issues, it was concluded that the conditions of the interface and viscosity can have a big impact on coalescence.

Since BSD can be impacted by operating conditions and physical properties, the impact of airflow rate and liquid viscosity was studied. In accordance to experimental observations, the model predicted that coalescence increases at higher airflow rates and decreases in more viscous solutions. When the airflow rate increases, a larger amount of gas enters the system, leading to a rise in the number of bubbles. This introduces more turbulence and increases the number of collisions, making coalescence events more likely to occur. Liquid viscosity was found to hamper turbulence because viscous forces impair the movement of bubbles through the continuous phase. Thus, the number of collisions diminishes, producing a decrease in the number of coalescence events.

In conclusion, a novel mathematical approach to predict BSD dynamics due to coalescence was proposed. The model was validated for the system studied by Amaral et al. (2018) and produced very good results, proving that it can be a powerful tool in predicting BSD dynamics. The implementation of this modelling approach in state-of-the-art oxygen transfer modelling can be the first step to improve the prediction of K_La, in turn, optimising the estimation of OTR in wastewater treatment. Therefore, this model can be a solution to the challenges imposed by high energy usages associated with aeration, leading to the mitigation of the environmental impact and an increase in cost-effectiveness of wastewater treatment plants.

5.2 Future perspectives

It has been reported that conditions of the interface can significantly affect the coalescence phenomenon. However, the state-of-the-art coalescence models do not usually consider its influence. Even though the model developed considered this effect, it was not possible to explicitly model it, as it was out of the scope of the experimental work developed by Amaral et al. (2018). Moreover, the influence of viscosity on the turbulent collision rate was found to be unknown. According to experimental data, viscosity significantly affects coalescence and, as such, the impact of this physical property on this phenomenon should be further studied. Therefore, future research should focus on studying the impact of conditions of the interface and viscosity, so that the current coalescence models can be refined.

To develop the model, there was a need to assume well-mixed conditions, since the FPT discards the PBM term that denotes the variation of number concentration due to advection in external coordinates. As studied in this work, this assumption is not verified in practice, as such, the model must be able to cope with a spatially variable number concentration profile. To accomplish that, the development of a CFD model that predicts the hydrodynamic regimes observed by Amaral et al. (2018) is needed. The coupling of this approach with the PBM model developed addresses the perfectly mixed conditions assumption.

Bibliography

Amaral, A.; Schraa, O.; Rieger, L.; Gillot, S.; Fayolle, Y.; Bellandi, G.; Amerlinck, Y.; Mortier, S. T.; Gori, R.; Neves, R., and Nopens, I. Towards advanced aeration modelling: From blower to bubbles to bulk. *Water Science and Technology*, 75(3):507–517, 2017.

Amaral, A.; Bellandi, G.; Rehman, U.; Neves, R.; Amerlinck, Y., and Nopens, I. Towards improved accuracy in modeling aeration efficiency through understanding bubble size distribution dynamics. *Water Research*, 131:346–355, 2018.

American Society of Civil Engineers. Development of standard procedures for evaluating oxygen transfer devices, 1983.

Bellandi, G.; Amerlinck, Y.; Hoey, S. V.; Amaral, A., and Nopens, I. Image analysis procedure to derive bubble size distributions for better understanding of the oxygen transfer mechanism. *IWA New Developments in IT & Water conference*, pages 1–4, 2016.

Bhole, M.; Joshi, J., and Ramkrishna, D. CFD simulation of bubble columns incorporating population balance modeling. *Chemical Engineering Science*, 63(8):2267–2282, 2008.

Bouaifi, M.; Hebrard, G.; Bastoul, D., and Roustan, M. A comparative study of gas hold-up, bubble size, interfacial area and mass transfer coefficients in stirred gas-liquid reactors and bubble columns. *Chemical Engineering and Processing*, 40(2):97–111, 2001.

Chaplin, F. M. Water: its Importance To Life. *Biochemistry and Molecular Biology Education*, 29(2): 54–59, 2001.

Chen, P.; Sanyal, J., and Duduković, M. P. Numerical simulation of bubble columns flows: Effect of different breakup and coalescence closures. *Chemical Engineering Science*, 60(4):1085–1101, 2005.

Deckwer, W. D.; Burckhart, R., and Zoll, G. Mixing and mass transfer in tall bubble columns. *Chemical Engineering Science*, 29(11):2177–2188, 1974.

Donckels, B. M. *Optimal experimental design to discriminate among rival dynamic mathematical models.* PhD thesis, Ghent University, 2009.

Durán, C.; Fayolle, Y.; Pechaud, Y.; Cockx, A., and Gillot, S. Impact of suspended solids on the activated sludge non-newtonian behaviour and on oxygen transfer in a bubble column. *Chemical Engineering Science*, 141:154–165, 2016.

Fayolle, Y.; Cockx, A.; Gillot, S.; Roustan, M., and Héduit, A. Oxygen transfer prediction in aeration tanks using CFD. *Chemical Engineering Science*, 62(24):7163–7171, 2007.

Gillot, S.; Capela-Marsal, S.; Roustan, M., and Héduit, A. Predicting oxygen transfer of fine bubble diffused aeration systems - Model issued from dimensional analysis. *Water Research*, 39(7):1379–1387, 2005.

Giri, A. K. and Hausenblas, E. Convergence analysis of sectional methods for solving aggregation population balance equations: The fixed pivot technique. *Nonlinear Analysis: Real World Applications*, 14(6):2068–2090, 2013.

Gleick, P. H. Water in Crisis: A Guide to the World's Fresh Water Resources, 1993.

Helser, J. *Monitoring, data analysis and modelling of gas-liquid mass transfer in wastewater treatment*. Master's thesis, Ghent University, 2018.

Jamialahmadi, M. and Muller-Steinhagen, H. Effect of superficial gas velocity on bubble Size, terminal bubble rise velocity and gas hold-up in bubble columns. *Developments in Chemical Engineering and Mineral Processing*, 1(1):16–31, 1993.

Jenkins, D. and Wanner, J. *100 Activated Sludge - 100 years and counting*. IWA Publishing, 2014.

Jiang, L. M.; Garrido-Baserba, M.; Nolasco, D.; Al-Omari, A.; DeClippeleir, H.; Murthy, S., and Rosso, D. Modelling oxygen transfer using dynamic alpha factors. *Water Research*, 124:139–148, 2017.

Jimenez, M.; Dietrich, N.; Grace, J. R., and Hébrard, G. Oxygen mass transfer and hydrodynamic behaviour in wastewater: Determination of local impact of surfactants by visualization techniques. *Water Research*, 58:111–121, 2014.

Karpinska, A. M. and Bridgeman, J. CFD-aided modelling of activated sludge systems - A critical review. *Water Research*, 88:861–879, 2016.

Kim, J. W. and Lee, W. K. Coalescence behavior of two bubbles in stagnant liquids. *Journal of Chemical Engineering of Japan*, 20(5):448–453, 1987.

Kumar, J.; Peglow, M.; Warnecke, G.; Heinrich, S., and Mörl, L. Improved accuracy and convergence of discretized population balance for aggregation: The cell average technique. *Chemical Engineering Science*, 61(10):3327–3342, 2006.

Kumar, S. and Ramkrishna, D. On the solution of population balance equations by discretization—I. A fixed pivot technique. *Chemical Engineering Science*, 51(8):1311–1332, 1996a.

Kumar, S. and Ramkrishna, D. On the solution of population balance equations by discretization—II. A moving pivot technique. *Chemical Engineering Science*, 51(8):1333–1342, 1996b.

Laakkonen, M.; Moilanen, P.; Alopaeus, V., and Aittamaa, J. Modelling local bubble size distributions in agitated vessels. *Chemical Engineering Science*, 62(3):721–740, 2007.

Lee, C.-H.; Erickson, L., and Glasgow, L. Bubble breakup and coalescence in turbulent gas-liquid dispersions. *Chemical Engineering Communications*, 59(1-6):65–84, 1987.

Liao, Y. and Lucas, D. A literature review on mechanisms and models for the coalescence process of fluid particles. *Chemical Engineering Science*, 65(10):2851–2864, 2010.

Lo, S. and Zhang, D. Modelling of breakup and coalescence in vertical bubbly two-phase flows. *Journal of Computational Multiphase Flows*, 1(1):23–38, 2009.

Maitland, P. *Biology of fresh waters*. Chapman and Hall, 1990.

Makinia, J. *Mathematical modelling and computer simulation of activated sludge systems*. IWA Publishing, 2010.

Metcalf and Eddy. *Wastewater engineering treatment and reuse*. McGraw-Hill, 2003.

Mihelcic, J. R. and Zimmerman, J. B. *Environmental engineering fundamentals, sustainability, design*. John Wiley & Sons, Inc., 2010.

Nopens, I. *Modelling the activated sludge flocculation process: A population balance approach*. PhD thesis, Ghent University, 2005.

Nopens, I.; Torfs, E.; Ducoste, J.; Vanrolleghem, P. A., and Gernaey, K. V. Population balance models: A useful complementary modelling framework for future WWTP modelling. *Water Science and Technology*, 71(2):159–167, 2015.

Peng, Y. Z.; Wang, X. L., and Li, B. K. Anoxic biological phosphorus uptake and the effect of excessive aeration on biological phosphorus removal in the A_2O process. *Desalination*, 189(1-3 SPEC. ISS.): 155–164, 2006.

Pittoors, E.; Guo, Y., and Van Hulle, S. W. Modeling dissolved oxygen concentration for optimizing aeration systems and reducing oxygen consumption in activated sludge processes: A review. *Chemical Engineering Communications*, 201(8):983–1002, 2014.

Prince, M. J. and Blanch, H. W. Bubble coalescence and breakup in air sparged bubble columns. *AIChE Journal*, 36(10):1485–1499, 1990.

Ramkrishna, D. The status of population balances. *Reviews in Chemical Engineering*, pages 49–95, 1985.

Ramkrishna, D. *Population balances theory and applicatons to particulate systems in engineering*. Academic Press, 2000.

Ramkrishna, D. and Singh, M. R. Population balance modeling: Current status and future prospects. *Annual Review of Chemical and Biomolecular Engineering*, 5(1):123–146, 2014.

Ratkovich, N.; Horn, W.; Helmus, F. P.; Rosenberger, S.; Naessens, W.; Nopens, I., and Bentzen, T. R. Activated sludge rheology: A critical review on data collection and modelling. *Water Research*, 47(2): 463–482, 2013.

Rehman, U.; Audenaert, W.; Amerlinck, Y.; Maere, T.; Arnaldos, M., and Nopens, I. How well-mixed is well mixed? Hydrodynamic-biokinetic model integration in an aerated tank of a full-scale water resource recovery facility. *Water Science and Technology*, 76(8):1950–1965, 2017.

Rosso, D. and Stenstrom, M. K. Economic implications of fine-pore diffuser aging. *Water Environment Research*, 78(8):810–815, 2006a.

Rosso, D. and Stenstrom, M. K. Surfactant effects on α-factors in aeration systems. *Water Research*, 40(7):1397–1404, 2006b.

Shah, Y. T.; Kelkar, B. G.; Godbole, S. P., and Deckwer, W. D. Design parameters estimations for bubble column reactors. *AIChE Journal*, 28(3):353–379, 1982.

Sommer, A. E.; Wagner, M.; Reinecke, S. F.; Bieberle, M.; Barthel, F., and Hampel, U. Analysis of activated sludge aerated by membrane and monolithic spargers with ultrafast X-ray tomography. *Flow Measurement and Instrumentation*, 53:18–27, 2017.

Surampalli, R. Y.; Tyagi, R. D.; Scheible, O. K., and Heidman, J. A. Nitrification, denitrification and phosphorus removal in sequential batch reactors. *Bioresource Technology*, 61(2):151–157, 1997.

Teixeira, J. A. and Fonseca, M. M. *Reatores biológicos*. Lidel, 2006.

Terashima, M.; So, M.; Goel, R., and Yasui, H. Determination of diffuser bubble size in computational fluid dynamics models to predict oxygen transfer in spiral roll aeration tanks. *Journal of Water Process Engineering*, 12:120–126, 2016.

Tsouris, C. and Tavlarides, L. L. Breakage and coalescence models for drops in turbulent dispersions. *AIChE Journal*, 40(3):395–406, 1994.

Van Daele, T. *Model-based analysis as a tool for intensification of a biocatalytic process in a microreactor*. PhD thesis, Ghent University, 2016.

Van Den Hengel, E. I.; Deen, N. G., and Kuipers, J. A. Application of coalescence and breakup models in a discrete bubble model for bubble columns. *Industrial and Engineering Chemistry Research*, 44 (14):5233–5245, 2005.

Wang, T. and Wang, J. Numerical simulations of gas-liquid mass transfer in bubble columns with a CFD-PBM coupled model. *Chemical Engineering Science*, 62(24):7107–7118, 2007.

Yeoh, G. H.; Cheung, C. P., and Tu, J. *Multiphase flow analysis using population balance modeling*. Elsevier, 2014.

A

Basic definitions of the PBM framework

In this annex, the notation and terminology necessary to comprehend the PBM framework and the formulation of the PBME are presented.

A.1 Particle State Vector

There are several internal properties that define the state of a particle in the same system, such as size, surface area, volume, composition, temperature, and so forth. However, depending on the application, not all these variables are adequate to describe the particle state. Hence, the main particle state variables must be chosen considering the nature of the process in hand. In general, the choice of the particle state is determined by the variables needed to specify: (1) The rate of change of those of direct interest to the application, (2) The birth and death processes.

It should be noted that the choice of the particle state by this general rule neglects memory effects.

Thus, the particle state variables considered must respect this restriction (Ramkrishna, 2000; Yeoh et al., 2014).

After choosing the adequate particle state variables, one can accommodate this information in a finite dimensional vector that can be used to characterise the particle state. This vector is composed of two different coordinates, external and internal. The former, represented by $\mathbf{r} \equiv (r_1, r_2, r_3)$, is used to denote the position vector of the particle as determined by that of its centroid. The latter, represented by $\mathbf{x} \equiv (x_1, x_2, \ldots, x_d)$, characterises the d different quantities associated with the particle (i.e. the *d* suitable internal properties). Therefore, the particle state vector is represented by ($\mathbf{x}$, $\mathbf{r}$), accounting for both external and internal coordinates (Ramkrishna, 2000; Yeoh et al., 2014). Finally, one can represent the domain of internal coordinates as V_x, which can be seen as an abstract property space, and the domain of external coordinates as V_r, which is a set of set of points in the physical space in which particles are present (Yeoh et al., 2014).

A.2 Continuous Phase Vector

The continuous phase variables, which affect the behaviour of each particle, can be assembled in a finite *c*-dimensional vector field named continuous phase vector. This vector is defined by $Y(\mathbf{r},t) \equiv [Y_1(\mathbf{r},t), Y_2(\mathbf{r},t), \ldots, Y_c(\mathbf{r},t)]$ and is a function of only the external coordinates $\mathbf{r}$ and time *t*. The calculation of the continuous phase vector is done using the governing transport equations and the boundary conditions associated with the particular problem. It should be noted that the continuous phase balance can be discarded if the interaction between the population and the continuous phase does not result in a significant change in the continuous phase. In these cases, the analysis of the population reduces to the PBME (Ramkrishna, 2000; Yeoh et al., 2014).

A.3 The Number Density Function

The number density function emerges from a postulation which states that there exists an average number density function defined on the particle state space. This assumption implies that the average number of particles of state ($\mathbf{x}$,$\mathbf{r}$) is $f_1(\mathbf{x},\mathbf{r},t)dV_x dV_r$. Besides that, the average number density function, $f_1(\mathbf{x},\mathbf{r},t)$, is considered to be a smooth function, which means that it can be differentiated with respect to any of its arguments as many times as necessary (Ramkrishna, 2000). The definition of the number density function allows the determination of the number of particles in any region of particle state space. Hence, the total number of particles in the entire system is given by equation (A.1) and the total number of particles per unit volume of physical space, denoted by $N(\mathbf{r},t)$, by equation (A.2) (Ramkrishna, 2000).

$$\int_{V_x} \int_{V_r} f_1(\mathbf{x}, \mathbf{r}, t)\, dV_x dV_r \tag{A.1}$$

$$N(\mathbf{x}, t) = \int_{V_x} f_1(\mathbf{x}, \mathbf{r}, t)\, dV_x \tag{A.2}$$

In equations (A.1) and (A.2), dV_x is the infinitesimal volume measure in the internal coordinates and dV_r in external coordinates (see section A.1).

Although the number density is one of the most used in the PBM framework, it is possible to define volume or mass density for the particle population as well. Since these densities are concerned with the amount of dispersed phase material, they are often more physically relevant than the number density (Ramkrishna, 2000). Despite the importance of both densities, only the volume density is addressed in this work because the deduction of the mass density is similar to that of the volume. Defining the volume of the particle of internal state **x** as $v(\mathbf{x})$, the volume density can be written as $v(\mathbf{x})f_1(\mathbf{x},\mathbf{r},t)$. Thus, the volume fraction density, ϕ $(\mathbf{x},\mathbf{r},t)$, of a particular state is defined by equation (A.3). On the other hand, considering the case of a scalar internal state using only particle size (volume) and denoting the number density by $f_1(\mathbf{v},\mathbf{r},t)$, the volume fraction density of particles of volume v is designed by equation (A.4).

$$\phi(\mathbf{x}, \mathbf{r}, t) = \frac{1}{\Phi(\mathbf{x}, t)} v(\mathbf{x}) f_1(\mathbf{x}, \mathbf{r}, t) \tag{A.3}$$

$$\Phi(\mathbf{x}, t) \equiv \int_{V_x} v(\mathbf{x}) f_1(\mathbf{x}, \mathbf{r}, t)\, dV_x \tag{A.4}$$

In equation (A.4), the denominator represents the total volume fraction of all particles (Ramkrishna, 2000).

A.4 The Rate of Change of Particle State Vector

The particle states can vary with time and, therefore, there is a need to define the rate of change of the particle state vector. The main concern is the smooth changes in particle state, which can be described by using separate velocity vectors, that are defined over the particle state space of both internal and external coordinates. The change of internal coordinates refers to motion through an abstract property space while the change of external coordinates refers to motion through physical space. Due to this distinction, one can define two separate velocities, $\mathbf{v}_x(\mathbf{x},\mathbf{r},\mathbf{Y},t)$ and $\mathbf{v}_r(\mathbf{x},\mathbf{r},\mathbf{Y},t)$, being the former related with the internal coordinates and the latter with the external coordinates. These functions are assumed to be as smooth as necessary and depend on the continuous phase, thus the presence of **Y**

in the functions' argument. Once the velocities through internal and external coordinates are characterised, it is possible to identify particle fluxes (number of particles per unit time per unit area normal to the direction of velocity). Hence, $f_1(\mathbf{x},\mathbf{r},t)\mathbf{v}_x(\mathbf{x},\mathbf{r},\mathbf{Y},t)$ is the particle flux through the internal coordinate space and $f_1(\mathbf{x},\mathbf{r},t)\mathbf{v}_r(\mathbf{x},\mathbf{r},\mathbf{Y},t)$ is the particle flux through the physical space. Both fluxes are evaluated at time t and at the point $(\mathbf{x},\mathbf{r})$ of the particle state space (Ramkrishna, 2000; Yeoh et al., 2014).

A.5 Particle State Continuum

The particle state continuum is a hypothetical material continuum that pervades the space of internal and external coordinates (Ramkrishna, 1985, 2000). The particles are considered to be firmly embedded in this continuum which can be viewed as deforming in space and time in accordance with the field $[\mathbf{v}_x(\mathbf{x},\mathbf{r},\mathbf{Y},t),\mathbf{v}_r(\mathbf{x},\mathbf{r},\mathbf{Y},t)]$ relative to the fixed coordinates (Ramkrishna, 2000; Yeoh et al., 2014). The introduction of this conceptual scenario facilitates the deduction of the PBE (Ramkrishna, 1985) because, under this continuum assumption, each particle phase is deemed to behave like a continuous fluid (Yeoh et al., 2014).

A.6 The Net Rate of Generation of Particles

Due to the assumption that the particles are firmly embedded in the deforming particle continuum, the integral formulation of the PBM states that the number of particles can only change through birth and death processes (Yeoh et al., 2014). Hence, there is a need to denote a function, usually referred to as h $(\mathbf{x},\mathbf{r},\mathbf{Y},t)$, as the net rate of generation of particles which represents the change in the density function attributed to particle break up/breakage and coalescence/aggregation (Yeoh et al., 2014). Even though in section 2.2.1 more evolutionary processes were mentioned, the only three considered by this function are the discrete ones (nucleation, break up/breakage, coalescence/aggregation) since these are the only ones that can change the number of particles in the system.